

Radio-frequency cascade readout of coupled spin qubits fabricated using a 300 mm wafer process

Jacob F. Chittock-Wood,^{1,2,*} Ross C. C. Leon,¹ Michael A. Fogarty,¹ Tara Murphy,^{1,3} Sofia M. Patomäki,^{1,2} Giovanni A. Oakes,¹ James Williams,^{1,2} Felix-Ekkehard von Horstig,^{1,3} Nathan Johnson,² Julien Jussot,⁴ Stefan Kubicek,⁴ Bogdan Govoreanu,⁴ David F. Wise,¹ John J. L. Morton,^{1,2,†} and M. Fernando Gonzalez-Zalba^{1,‡}

¹ Quantum Motion, 9 Sterling Way, London N7 9HJ, United Kingdom

² London Centre for Nanotechnology, UCL, London WC1H 0AH, United Kingdom

³ Department of Materials Sciences and Metallurgy, University of Cambridge, Cambridge CB3 0FS, United Kingdom

⁴ IMEC, Kapeldreef 75, 3001 Leuven, Belgium

Advanced semiconductor manufacturing offers a promising path to scaling up silicon-based quantum processors by improving yield, uniformity, and integration. Individual spin qubit control and readout have been demonstrated in quantum dots fabricated using 300 mm wafer metal-oxide-semiconductor (MOS) processes, yet quantum processors require two-qubit interactions to operate. Here, we use a 300 mm natural silicon MOS process customised for spin qubits and demonstrate coherent control of two electron spins using the exchange interaction, forming the basis for entangling gates such as $\sqrt{\text{SWAP}}$. We measure gate dephasing times of up to $T_2^* \approx 500$ ns with a quality factor of 10. For readout, we introduce a novel dispersive readout technique, the radio-frequency electron cascade, that simplifies the qubit unit cell while providing high gain. This method achieves an SNR of 6 in 46 μs , the highest-performing dispersive readout demonstration in a planar MOS process. The combination of sensitive dispersive readout with industrial-grade manufacturing marks a crucial step towards large-scale integration of silicon quantum processors.

Silicon-based quantum processors have recently demonstrated high-fidelity qubit initialisation [1, 2], measurement [3–5], and single-[6–8] and two-qubit control [9–14] in small-scale devices of up to two qubits, with fidelities exceeding the 99% threshold required to implement quantum error correction [15]. Further progress has been achieved using electron spin qubits in quantum dots (QDs). In particular, simple instances of quantum error correction have been demonstrated in a 3-qubit array [2], and a 6-qubit processor has been successfully operated [16]. As the technology matures, it is crucial to take advantage of the manufacturing capabilities of the semiconductor industry to scale up to larger arrays of qubits. This approach promises to facilitate integration with classical electronics for control and readout, paving the way for an integrated quantum computing system [17–19].

Spin qubits based on silicon metal-oxide-semiconductor (MOS) technology [20, 21] and Si/SiGe heterostructures [11, 16, 22–24] are of particular interest for industrial manufacturing. Specifically, the MOS approach shares similarities with modern silicon field-effect transistor (FET) manufacturing, enabling the formation of MOS QDs in both planar devices [13, 20, 21, 25–27], and etched silicon structures, such as nanowires [4, 28, 29] or finFETs [6, 30]. While the latter constrains the qubit topology to 2xN bilinear QD arrays, the former offers easier scalability towards two-dimensional QD arrays [31], which are essential for implementing quantum

error correcting codes such as the surface code [15]. This potential for scaling has driven the translation of the well-established operation of high-quality qubits within academic MOS devices [8, 13, 20, 25, 26], to demonstrations of single-qubit performance in MOS devices fabricated using semiconductor manufacturing lines [28, 30]. Yet, quantum processors require two-qubit interactions to operate.

To enable further scaling, methods that simplify the readout infrastructure must be developed. The current standard for sensing, the radio-frequency single-electron transistor, offers high-fidelity readout [3, 5] at the cost of occupying substantial space on the qubit chip, which limits qubit connectivity. To address this limitation, efforts have focused on integrating fast and compact radio-frequency measurement techniques [32–34], which substantially reduce the readout footprint. However, despite recent advances in other areas, dispersive readout metrics have seen little progress in planar MOS in recent years [33].

In this Article, we study electron spins within a silicon double quantum dot (DQD) device fabricated using a 300 mm wafer line [35, 36] to address the two aforementioned outstanding challenges: First, we introduce a new in situ dispersive sensing mechanism (termed *radio-frequency electron cascade*) which offers enhanced sensitivity for spin qubit readout. We achieve a minimum integration time of 8 μs and, using a physical model [37], we calculate a 67% singlet-triplet readout fidelity limited by spin relaxation. Second, we demonstrate control of an exchange-mediated coherent interaction, which forms the basis for a $\sqrt{\text{SWAP}}$ gate between two spin qubits.

* jacob.chittock-wood.15@ucl.ac.uk

† john@quantummotion.tech

‡ fernando@quantummotion.tech

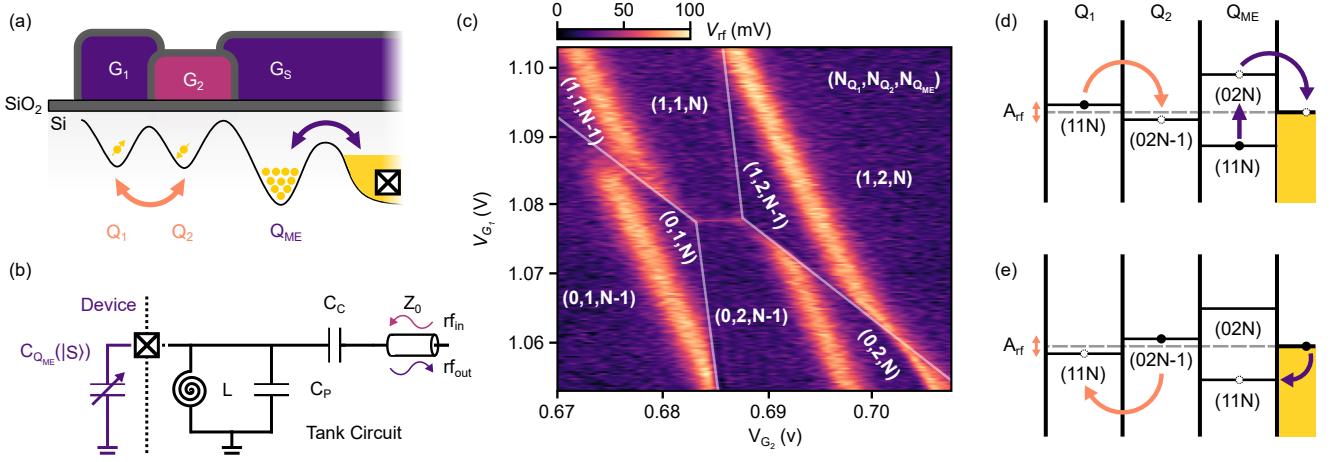


Fig. 1. | **Radio-frequency driven electron cascade.** **a**, Cross-section schematic of the quantum dot array. Gates G_1 and G_2 define QDs, Q_1 and Q_2 , tuned to the two-electron occupancy. The DQD is capacitively coupled to dot Q_{ME} occupied with many electrons and is controlled by gate G_S . Arrows indicate single electron tunnelling events. **b** Schematic of the rf resonator bonded to the reservoir contact of the device, including a circuit equivalent representation of the QD array as a spin dependent variable capacitor $C_{Q_{ME}}(|S|)$. The resonator is formed by an off-chip superconducting spiral inductor, $L = 136$ nH, arranged in parallel with the parasitic capacitance, $C_P = 0.4$ pF, of the assembly. Connected to the transmission line Z_0 , via coupling capacitor $C_C = 0.1$ pF. **c**, Charge stability diagram of the DQD. **d-e**, Schematic representations of the cascade process in which the rf excitation synchronously drives charge transitions within the QD array. **d**, A change in the charge configuration of the DQD from $(1,1)$ to $(0,2)$ raises the electrochemical potential of the Q_{ME} above the Fermi level, causing one electron to synchronously escape to the reservoir. **e**, When the DQD is driven back to $(1,1)$, an electron tunnels back from the reservoir to Q_{ME} .

RADIOFREQUENCY ELECTRON CASCADE READOUT

Reading out spin qubits within semiconductor QDs typically involves mapping a spin state of interest onto a charge state of one or more QDs [38, 39], which can then be detected using a variety of charge sensing methods [40]. For example, Pauli spin blockade (PSB) can be used to map the singlet and triplet states of a pair of spin qubits onto two different charge configurations of a DQD (e.g. $(1,1)$ or $(0,2)$), which are then detected by a single electron transistor [41] or single electron box [4]. *In-situ* dispersive readout of a DQD combines these into a single step, using PSB to directly distinguish between singlet and triplet states through their difference in AC polarisability [42]. This difference in polarisability is detected by incorporating the DQD into a radiofrequency (rf) tank circuit and measuring changes in the reflected rf signal. However, *in-situ* dispersive readout has suffered from low sensitivity in planar MOS silicon quantum devices due to the relatively low gate lever arms [33]. To improve the sensitivity of this technique, we introduce a third quantum dot (QD) coupled to a charge reservoir, which acts as an amplifier in measuring the AC-polarisability of the DQD. Instead of measuring the usual single-electron alternating current generated by the cyclic tunneling between the two-spin singlet states of the DQD [40], we leverage the *synchronised* single-electron AC current at the third dot-reservoir system generated as a consequence of the strong capacitive coupling to the

DQD. Our approach offers the benefit of charge enhancement techniques such as latching [43], DC cascading [44] and spin-polarized single-electron boxes [45] while retaining the non-demolition nature of *in-situ* dispersive readout methods [46].

We use a device based on planar silicon MOS technology with an overlapping gate design [36] (see Fig 1(a)). Quantum dots Q_1 and Q_2 form a DQD which we tune to hold two electrons, while Q_2 is capacitively coupled to a multi-electron quantum dot (Q_{ME}) that can exchange electrons with a charge reservoir. To measure the charge state of the system, we connect a superconducting spiral inductor to the reservoir, forming a LC resonator (see Fig. 1(b)). At voltages where the charge in Q_{ME} is bistable, cyclic tunneling generated by the small rf signal supplied to the resonator produces a change in capacitance that can be detected as a change in the phase response, $\Delta\Phi$, using homodyne techniques [40]. Lines in gate voltage space showing Q_{ME} charge bistability are shifted when intersecting charge transitions of the DQD, as shown in Fig. 1(c). Such shifts form the basis of dispersive charge sensing measurements [4, 49, 50] which we do not exploit here. Instead, we focus on the directly observable AC signal in the region of gate voltage space where charge transitions may occur between Q_1 and Q_2 . We ascribe this signal to a two-electron charge cascade effect driven by the rf excitation, which we explain using the diagrams in Fig. 1(d-e). Consider an rf cycle in which the system starts in the occupation configuration $(N_{Q_1}, N_{Q_2}, N_{Q_{ME}}) = (1, 1, N)$. Due to the strong capac-

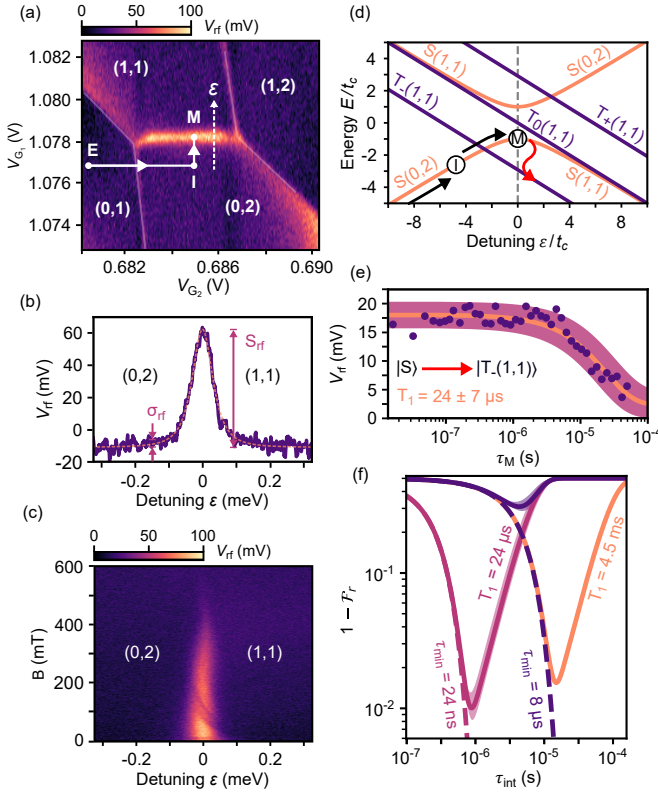


Fig. 2. | **Radio-frequency cascade readout fidelity.** **a** Charge stability diagram of the DQD around the (1,1)-(0,2) interdot charge transition (ICT), with a voltage pulse sequence and detuning axis ε overlaid **b** Energy diagram showing dependence of the two-electron spin states, singlet $|S\rangle$ and triplet $|T\rangle$ as a function of ε . The pulse sequence depicts the initialisation (I) of the $|S(0,2)\rangle$ via an adiabatic ramp from the (0,1) empty (E) state, followed by a non-adiabatic pulse to $\varepsilon = 0$ for measurement (M). **c**, Reflected resonator voltage V_{rf} as a function of detuning across the ICT around $\varepsilon = 0$, fit to Eq. (4) (dashed orange line). **d**, Magneto-spectroscopy of the interdot charge transition of the DQD along detuning, ε . **e**, V_{rf} as a function of wait time τ_M at $\varepsilon = 0$ before measurement, following the pulse sequence depicted in panels **a** and **c**. The fitted line indicates a $|S\rangle$ to $|T_{-}(1,1)\rangle$ relaxation time $T_1 = 24 \mu\text{s}$. **f**, Calculated readout infidelity $1 - \mathcal{F}_r$ as a function of integration time τ_{int} as described by Eq. (7). Solid lines depict relaxation time T_1 limited fidelity, whereas dashed lines depict $T_1 = \infty$. Parameters used from left to right include: $\tau_{\text{min}} = \{23 \text{ ns}, 8 \mu\text{s}, "\}$, $T_1 = \{24 \mu\text{s}, " , 4.5 \text{ ms}\}$.

itive coupling between Q_2 and Q_{ME} , the rf excitation that drives the DQD from the (1,1) to (0,2) state synchronously forces an electron out of Q_{ME} in a cascaded manner, leading to (0,2, $N - 1$). The second half of the rf cycle then reverses the process. Overall, the rf cascade measures the polarizability of the DQD system, as for *in-situ* dispersive readout measurements [33, 34], but with the substantial advantage that the induced charge can be much greater, resulting in a dispersive measurement with greater sensitivity (see Supplementary Section S1

for more discussion on the requirements for rf electron cascade readout). Specifically, we find the power signal is amplified in the cascade approach compared to direct dispersive readout, by a factor

$$A = \left(1 + \frac{1 - \alpha_{\text{R,ME}}}{\alpha_{\text{R,2}} - \alpha_{\text{R,1}}}\right)^2 > 1, \quad (1)$$

where $\alpha_{\text{R},j}$ represents the gate lever arm between the reservoir and QD j . In particular, the sensor detects not only the interdot gate polarization charge $(\alpha_{\text{R,1}} - \alpha_{\text{R,2}})e$ but also the cascaded charge collected at the reservoir, $(1 - \alpha_{\text{R,ME}})e$, (see Supplementary Section S2 for derivation). By comparing the measured signal-to-noise ratio (SNR) with and without the cascade effect, we find a lower bound for the power amplification factor, $A \geq (3.4 \pm 0.1) \times 10^3$ (+35.4 dB). The cascade SNR is extracted from the interdot charge transition fit shown in Fig. 2(a-b) (see Eq. (4-5) in Methods). For the case where the cascade is absent, the SNR is assumed to be 0.5, as there is no observable signal, as shown in Supplementary Fig. S1(a) and (e). From the cascade SNR we extract a minimum integration time of $\tau_{\text{min}} = 7.6 \pm 0.2 \mu\text{s}$ (see Eq. (6) in Methods), representing an improvement of over two orders-of-magnitude on prior planar MOS demonstrations of *in-situ* dispersive readout [33].

We use the rf-cascade to distinguish between the singlet and triplet states of the DQD via PSB. The signature of PSB can be observed by measuring the asymmetric disappearance of the interdot charge transitions as a function of increasing the applied magnetic field [42], as shown Fig. 2(c). At low magnetic field ($B \leq 200 \text{ mT}$), the system is free to oscillate between singlet states ($|S(1,1)\rangle \leftrightarrow |S(0,2)\rangle$) due to the action of the rf drive, yielding a signal in the rf response. However, at higher fields ($B \geq 200 \text{ mT}$), the polarised triplet $|T_{-}(1,1)\rangle$ state becomes the ground state for $\varepsilon \geq 0$ (as shown in Fig. 2(d)), preventing a charge transition and resulting in the disappearance of the signal, initially for the region of the transition closer to the (1,1) charge configuration. A quantum capacitance-based simulation of the data in the inset suggests an inter-dot tunnel coupling of $t_c = 2.4 \text{ GHz}$ and electron temperature $T_e = 50 \text{ mK}$ (see Supplementary Section S4). Figure 2(e) shows the decay from $|S\rangle$ to $|T_{-}(1,1)\rangle$ at $\varepsilon = 0$ for applied magnetic field $B = 250 \text{ mT}$. The corresponding relaxation time is $T_1 = 24 \pm 7 \mu\text{s}$, which is consistent with a study of a similar device, where a relaxation time of $T_1 = 10 \mu\text{s}$ was observed near zero detuning for a comparable tunnel coupling ($t_c \geq 1.9 \text{ GHz}$) [51]. In that study, T_1 was found to vary exponentially with t_c , with relaxation times exceeding $200 \mu\text{s}$ for $t_c \leq 1 \text{ GHz}$. Lowering t_c would also enhance the readout sensitivity, as the dispersive signal is maximised at $2t_c = f_{\text{rf}}/2$ [?], where f_{rf} is the resonator drive frequency, which we set to 512 MHz .

We assess the performance of the radio-frequency driven electron cascade by calculating the readout fidelity, \mathcal{F}_r as a function of integration time, using Eq. (7)

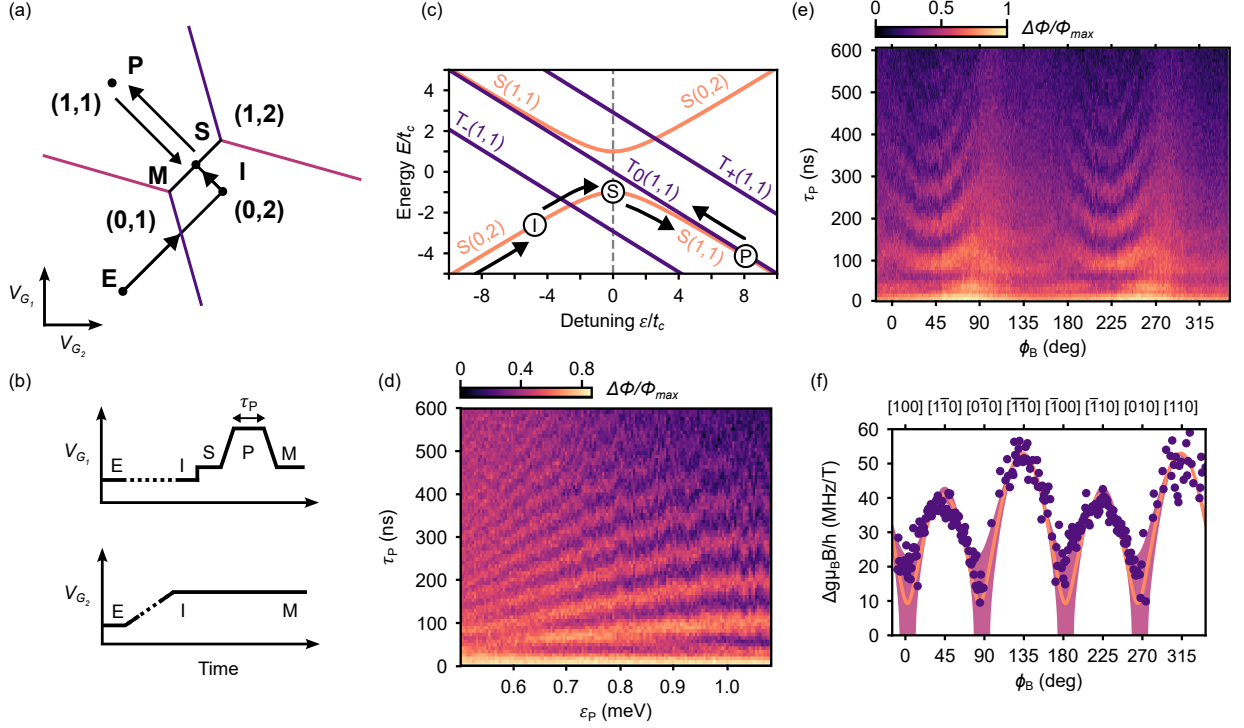


Fig. 3. | **Measurement of the spin-orbit interaction.** **a**, Schematic of the DQD charge stability diagram around the (1,1)-(0,2) interdot charge transition with voltage pulse sequence overlaid (shown also as a function of time in panel **b**, where dashed lines indicate longer durations). **c**, Energy diagram showing dependence of the two-electron spin states, singlet $|S\rangle$ and triplet $|T\rangle$ as a function of detuning ϵ . **d**, $|S\rangle$ - $|T_0\rangle$ oscillations as a function of duration τ_P and detuning at point P ϵ_P in the pulse sequence ($B = 250$ mT, $\phi_B = 235^\circ$). **e-f**, $|S\rangle$ - $|T_0\rangle$ oscillation frequency dependence as a function of the in-plane magnetic field orientation ϕ_B , measured at fixed detuning $\epsilon_P = 0.926$ meV. The fit in **f** is obtained using the spin-orbit interaction model described in Eq. (2) and incorporates the error in σ_{HF} and $J(\epsilon_P)$.

in Methods [37]. We calculate a relaxation-limited readout fidelity of $\mathcal{F}_r = 67 \pm 1\%$ based on the experimentally obtained $\tau_{\min} = 7.6$ μ s and integration time $\tau_{\text{int}} = 8$ μ s. The corresponding readout infidelity $1 - \mathcal{F}_r$ is depicted in Fig. 2(f) (dark purple line). This infidelity is a comparable order of magnitude to prior *in-situ* readout demonstrations, but is achieved with integration times that are 1-2 orders of magnitude faster than those reported in previous silicon planar MOS and implanted donor systems [32, 33] (see Supplementary Table I). To achieve a 99% fidelity, two strategies are indicated in Fig. 2(f): (i) reducing the minimum integration time to 24 ns (light purple line), by enhancing the SNR through resonator optimisation or quantum-limited amplification [40, 52]; and (ii) by extending the relaxation time of the system, which for the $T_1 = 4.5$ ms reported in [33] yields the orange line.

We highlight that, unlike other charge enhancement techniques [43–45], the rf electron cascade retains the non-demolition nature of *in-situ* dispersive readout measurements since the DQD system remains in an eigenstate after a measurement is performed [1, 53]. We note that the rf excitation is continuously applied for all measurements in this Article, we discuss the potential impact of this in the echo sequence section.

CHARACTERISING SPIN-ORBIT COUPLING

Having established a method to distinguish between singlet and triplet spin states, our goal is to prepare and coherently control spin states of the DQD through voltage pulses along the detuning axis, ϵ . Such pulses bring the DQD: i) from the (0,2) charge configuration in which a singlet is prepared; ii) into the (1,1) region where the electron spins are spatially separated between QDs and may evolve; and iii) back to an intermediate point where they can be measured (see Fig. 3(a-c)). Deep in the (1,1) region, the spin basis states are predominantly $|\uparrow\downarrow\rangle$ and $|\downarrow\uparrow\rangle$. Under an adiabatic ramp to $\epsilon = 0$ for readout, these two states map onto the $|T_0(1,1)\rangle$ and $|S(0,2)\rangle$, respectively. The basis states are separated in energy by $\hbar\Omega = \sqrt{J(\epsilon)^2 + \Delta E_z^2}$, where we include the kinetic exchange interaction $J(\epsilon)$ and the Zeeman energy difference between electrons in each dot ΔE_z . The spin detuning $\Delta E_z = \Delta g \mu_B B + g \mu_B \Delta B_{HF}$ (where μ_B is the Bohr magneton, h is Planck's constant) contains two main contributions: (i) the difference in g-factor between QDs $\Delta g = |g_2 - g_1|$ arising from variations in the spin-orbit interaction (SOI) present near the Si/SiO₂ interface [26, 54, 55]; and (ii) the difference in the effective ^{29}Si nuclear magnetic field experienced by each

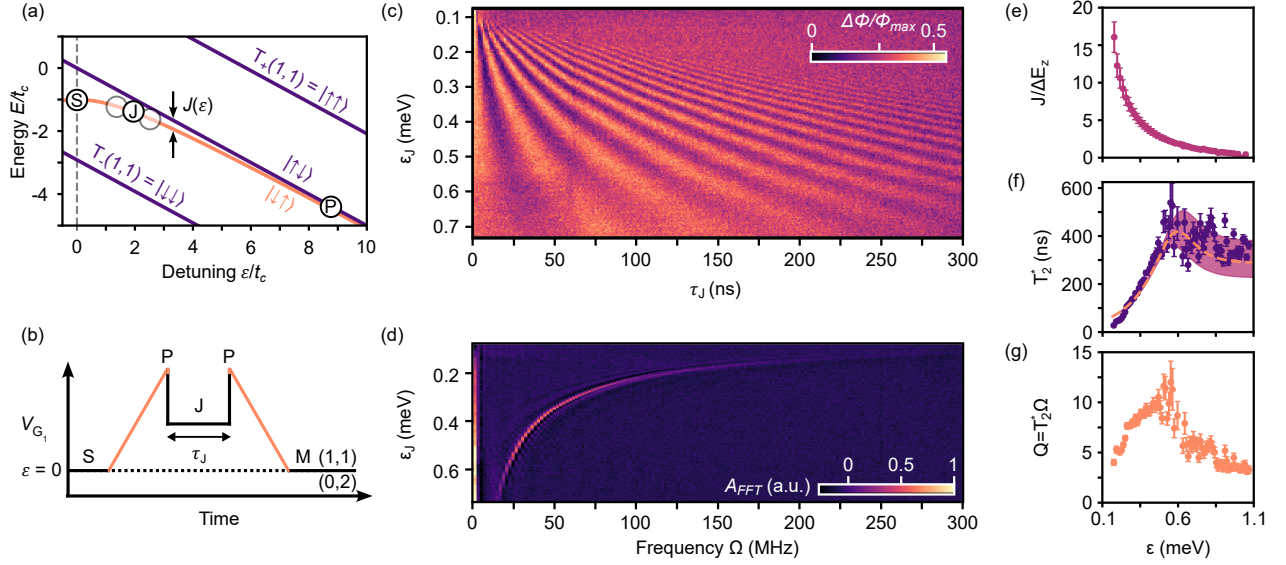


Fig. 4. | **Exchange control in the ^{nat}Si double quantum dot device.** **a**, Energy diagram depicting two-electron spin states in the (1,1) detuning regime, with pulse sequence steps overlaid. **b**, Detuning pulse sequence including initialisation to the $|\downarrow\uparrow\rangle$ state via a semi-adiabatic ramp (orange), followed by a non-adiabatic pulse (J) to near zero-detuning to increase the exchange coupling for duration τ_E . **c**, Exchange driven oscillations between $|\downarrow\uparrow\rangle$ and $|\uparrow\downarrow\rangle$ states, measured rf-phase response proportional to singlet probability, with **d**, the corresponding Fourier transform. **e** Ratio between exchange coupling strength $J(\epsilon)$ and dot-to-dot Zeeman energy difference ΔE_z . **f** Dephasing time T_2^* extracted from the decay of the exchange oscillations (orange dots) and fit with $T_2^* = \sqrt{2\hbar}/\delta(\hbar\Omega)$ (purple line) [47, 48]. **g** Qubit quality factor. Error bars indicate standard deviation of each data point.

QD, ΔB_{HF} . The random fluctuations in the effective magnetic field experienced by each electron in the DQD can be described by a normal distribution with mean of 0 (given the negligible spin polarisation) and standard deviation $\sigma_{\text{HF}} = 30 \pm 4 \mu\text{T}$, as we shall see later. This value corresponds to a hyperfine energy strength of $3.4 \pm 0.4 \text{ neV}$, which aligns well with other reports in natural silicon [22, 48, 56, 57].

In prior work, the spin detuning ΔE_z has been leveraged to drive oscillations between $|S\rangle$ and $|T_0\rangle$ states [26, 27, 57, 58]. At an applied magnetic field $B = 250 \text{ mT}$, we observe similar oscillations using the pulse sequence presented in Fig. 3(a-c): We start in the (0,1) configuration by emptying dot Q_1 , then initialise the $|S(0,2)\rangle$ state via an adiabatic ramp across the (0,1)-(0,2) charge transition. A fast non-adiabatic pulse to ϵ_P in the (1,1) region leads to oscillations between $|S\rangle$ and $|T_0\rangle$ over the course of the dwell time τ_P . The final state is then measured dispersively using a non-adiabatic pulse back to the (1,1)-(0,2) charge transition at $\epsilon = 0$ for readout. The $|S\rangle$ - $|T_0\rangle$ oscillations shown in Fig. 3(d) provide a direct measurement of Ω . For $\epsilon_P \gtrsim 0.9 \text{ meV}$ the dependence of the oscillation frequency on detuning is significantly reduced, suggesting that in this region the ΔE_z term dominates ($J(\epsilon) \leq \Delta E_z$), since Δg is only weakly dependent on detuning ($\partial\Delta g/\partial\epsilon \approx 0$) [27, 58]. As we shall see later, at the deepest detuning ($\epsilon_P = 1.054 \text{ meV}$), we find $J/\Delta E_z = 0.5 \pm 0.3$.

The strength of the SOI which leads to the Δg term depends on Rashba and Dresselhaus spin-orbit couplings.

The SOI (and hence Δg) can be tuned by varying the electrostatic confinement perpendicular to the interface and the transverse magnetic field [26, 54]. We vary the orientation of the in-plane magnetic field and observe changes in the $|S\rangle$ - $|T_0\rangle$ oscillation frequency, as shown in Fig. 3(e-f). We fit the variation in Ω as a function of the angle, ϕ_B , between the [100] crystal axis and the applied (in-plane) magnetic field [26],

$$\Delta E_z/h = \sqrt{(|B| |\Delta\alpha - \Delta\beta \sin(2\phi_B)|)^2 + (g\mu_B\sigma_{\text{HF}}/h)^2}. \quad (2)$$

The Rashba and Dresselhaus SOI terms are respectively captured by $\Delta\alpha$ and $\Delta\beta$. We find $\Delta\alpha = 6.2^{+1.6}_{-1.5} \text{ MHz/T}$ and $\Delta\beta = 45^{+5}_{-7} \text{ MHz/T}$, which are larger than other reported values [26, 55, 59] and could be partially influenced by the large asymmetry in the gate biasing conditions. The fit assumes that for the fixed detuning of $\epsilon_P = 0.926 \text{ meV}$ used here, the residual exchange interaction $J(\epsilon_P)/h = 6.3 \pm 1.9 \text{ MHz}$ is independent of in-plane magnetic field orientation. We operate at an in-plane magnetic field direction near the $[1\bar{1}0]$ direction at $\phi_B = 55^\circ$ (235°). Overall, this section expands the recent studies of the SOI in isotopically purified ^{28}Si MOS nanostructures [26, 27, 55, 59] to natural silicon, where the non-negligible effect of the Overhauser field needs to be taken into account.

EXCHANGE CONTROL

We implement exchange control using the sequence depicted in Fig. 4(a,b), where the $|\downarrow\uparrow\rangle$ state is initialised via a ramp from $\varepsilon = 0$ into the (1,1) configuration that is adiabatic with respect to E_z [22, 60]. A fast non-adiabatic pulse towards zero detuning increases the exchange coupling, driving oscillations between the $|\downarrow\uparrow\rangle$ and $|\uparrow\downarrow\rangle$ states at frequency $\Omega(\varepsilon)$, as observed in Fig. 4(c). The final state after some evolution time τ_J is projected to $|S\rangle$ or $|T_0\rangle$ for readout. The Fourier transform of the exchange oscillations (see Fig. 4(d)) reveals a single peak of increasing frequency as the detuning is reduced, indicating the purity of the oscillations and the enhanced exchange strength at lower detuning. From this, we observe that the exchange coupling is tunable over a range of $J = 5 - 122$ MHz.

To quantify the properties of these rotations, we combine the results of the exchange oscillations in Fig. 4(c) and the $|S\rangle$ - $|T_0\rangle$ oscillations in Fig. 3(d), to extract the ratio $J/\Delta E_z$ and the intrinsic coherence time T_2^* over a wide range of detunings, see Fig. 4(e,f). We extract T_2^* by fitting the oscillations at each detuning point with a Gaussian decay envelope of the form $\exp[-(\tau/T_2^*)^2]$, and then obtain $\Delta E_z = 9.6 \pm 1.2$ MHz from the fit to the expression

$$\frac{1}{T_2^*} = \frac{1}{\sqrt{2}\hbar} \sqrt{\left(\frac{J}{\hbar\Omega} \frac{dJ}{d\varepsilon} \delta\varepsilon_{\text{rms}}\right)^2 + \left(\frac{\Delta E_z}{\hbar\Omega} \delta\Delta E_{z,\text{rms}}\right)^2}, \quad (3)$$

where $\delta\varepsilon_{\text{rms}}$ and $\delta\Delta E_{z,\text{rms}}$ refer to the root mean square of the fluctuations in ε and ΔE_z [47, 48].

The extracted $J/\Delta E_z$ ratio is shown in Fig. 4(e), reducing as a function of increasing ε to a minimum value of 0.5 ± 0.3 at $\varepsilon = 1.054$ meV (beyond this point we cease to observe oscillations). This non-zero minimum shows there remains a residual exchange that cannot be fully turned off, which should be taken into account when designing two-qubit exchange gates.

From the T_2^* data shown in Fig. 4(f), we observe a rapid increase in coherence as the detuning increases from zero, indicative of a low $\delta\varepsilon_{\text{rms}}$. The extracted value of $\delta\varepsilon_{\text{rms}} = 5.4 \pm 0.1$ μeV , obtained over a measurement time of 0.3 h per trace, is at the state-of-the-art for MOS devices [25, 26, 57], and can be attributed to the low charge noise achieved for samples using this 300 nm process [35], comparable to reports on SiGe heterostructures [61, 62] (see Methods). As the detuning increases further, where $J < \Delta E_z$, we observe that noise in ΔE_z dominates (due to ^{29}Si nuclear spins), leading to a relatively constant T_2^* . From this saturation value of $T_2^* = 0.28 \pm 0.04$ μs , we extract $\sigma_{\text{HF}} = \sqrt{2\pi\delta\Delta E_{z,\text{rms}}/(g\mu_B)} = 30 \pm 4$ μT . Note that we assume the Zeeman energy fluctuations are dominated by the Overhauser field rather than noise in the g factor difference.

The entangling two-qubit gate achieved between the spin qubits under the exchange interaction depends on

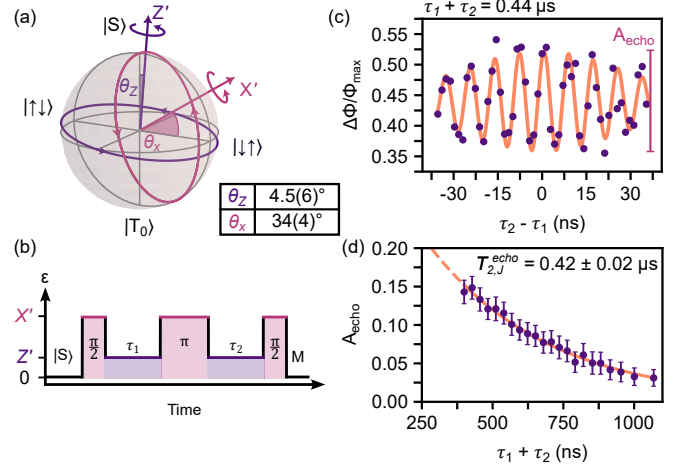


Fig. 5. | **Echo sequence.** **a**, Bloch sphere representation of the odd-parity two spin sub-space, indicating the rotation axes, \hat{Z}' and \hat{X}' and their angular deviation from the nominal \hat{Z} axis defined by $|S\rangle$ and $|T_0\rangle$. **b**, Schematic of the exchange echo sequence. **c**, Echo signal as a function of free evolution time difference $\tau_2 - \tau_1$. **d**, Echo amplitude as a function of total free evolution time $\tau_2 = \tau_1$. Data (purple dots) with standard deviation and exponential decay fit (orange line).

the ratio $J/\Delta E_z$, tending to a $\sqrt{\text{SWAP}}$ operation as $J \gg \Delta E_z$ or a C-PHASE when $J \ll \Delta E_z$, though any gate within this set parameterised by $J/\Delta E_z$ can be used as the building block for a quantum error correcting code such as the surface code [63]. Defining the qubit quality factor as $Q = T_2^* \Omega$ (i.e. the number of periods before the amplitude of oscillations decays by $1/e$), we find $Q \gtrsim 10$ in the region $J/\Delta E_z = 2.1 - 3.2$, on par with prior reports across a range of semiconductor platforms [26, 47, 48, 56, 58]. This provides an upper bound estimate on the achievable two-qubit gate fidelity using the approximation $\mathcal{F} \approx 1 - 1/4Q \gtrsim 98\%$ [64]. To implement error-correctable two-qubit gates this fidelity would need to surpass 99% [15], which could be achieved using isotopically enriched silicon. In the next section, we extend the coherence time using spin refocusing techniques.

ECHO SEQUENCE

Dephasing of the two-electron spin state due to low-frequency electric or magnetic noise can be corrected using refocusing pulses. We implement an echo sequence by combining periods of evolution at different detuning points in order to achieve rotations around the two axes, Z' and X' shown in Fig. 5(a). The specific sequence shown in Fig. 5(b), termed the exchange echo, primarily reduces the impact of electric noise [26, 47].

In the exchange echo sequence, after initialising a $|S(1,1)\rangle$ state and applying a $X'_{\pi/2}$ rotation, the two-electron system dephases under the effect of charge noise

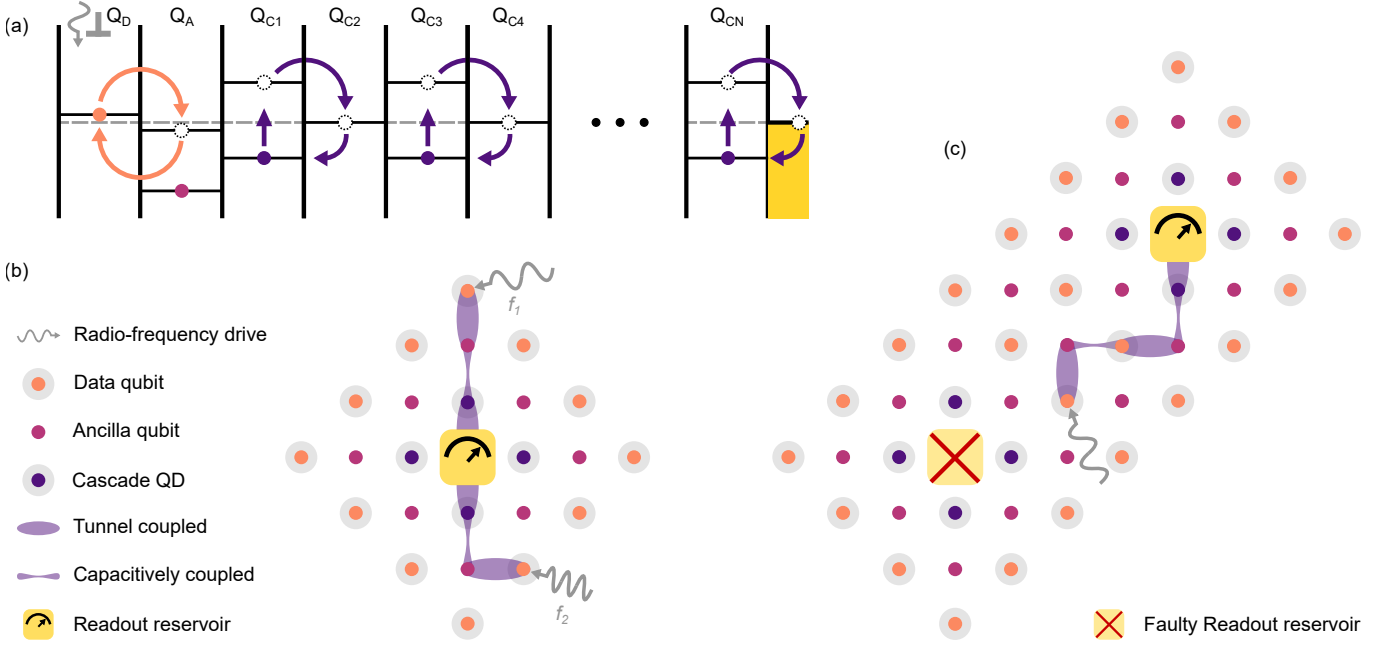


Fig. 6. | **Extending radio-frequency cascade readout to two-dimensional arrays.** **a**, Schematic representation of the cascade process extended to an arbitrarily long one-dimensional array. Pauli spin blockade readout is achieved by tunnel coupling the data Q_D (orange) and ancilla Q_A qubit (light purple), the resulting DQD is capacitively coupled to a chain of DQDs tuned into the cascade configuration (Q_{CN}) (dark purple). Enabling in-situ dispersive readout at an arbitrary distance. **b**, Two-dimensional array schematic unit-cell centred around a readout reservoir (yellow), connected to a radio-frequency reflectometry readout apparatus. Simultaneous multiplexed readout is achieved by applying distinct rf frequencies f_1 and f_2 to separate electrostatic gates, each controlling data qubit QDs, driving distinct cascaded charge transitions. **c** Repetition of the unit cell highlighting the robustness of the scheme to points of failure, such as a faulty readout reservoir, by re-routing the readout cascade chain to the nearest reservoir.

for a time τ_1 . The free evolution occurs at a detuning point where $J/\Delta E_z = 12.8 \pm 1.6$ where we measured $T_2^* = 43 \pm 3$ ns (see Fig 4(f)). We then refocus the spins by applying a X'_π rotation and let the system evolve for τ_2 until a second $X'_{\pi/2}$ rotation maps the resulting state to the $|S\rangle$ - $|T_0\rangle$ axis. We extract the amplitude of the echo by fitting the signal in the $\tau_2 - \tau_1$ domain (see Fig. 5(c)), and plot its value as a function of total free evolution time $\tau_1 + \tau_2$. Fig. 5(d) shows the echo amplitude decays exponentially with total time ($\tau_2 + \tau_1$), yielding a characteristic $T_{2,J}^{\text{echo}} = 0.42 \pm 0.02$ μs which corresponds to an order of magnitude increase in the coherence time, similar to prior work with silicon devices [26, 56]. From our fit to Eq. (3), we extract a magnetic-noise-limited $T_{2,\Delta E_z}^* = 3.3$ μs at this set point, indicating that sources other than magnetic noise limit $T_{2,J}^{\text{echo}}$. This finding is in agreement with previous reports, which show that $T_{2,J}^{\text{echo}}$ is an order of magnitude shorter than the magnetic noise limit [26, 56] (see Supplementary Table II). We speculate that residual high-frequency charge noise limits the echo coherence [7]. This noise may include factors such as the effect of the rf readout excitation, which is active throughout the control sequence. We estimate the upper-bound on detuning fluctuations associated with this rf excitation to be $\delta\epsilon_{\text{rms}}^{\text{rf}} \leq 2.7$ μeV (see Methods Eq. (8)).

However, this limitation is not intrinsic to the the readout scheme itself, as the effect can be effectively mitigated by implementing a pulsed readout protocol. In this approach, the rf-drive is deactivated during the control sequence, and only activated during the readout phase [65].

DISCUSSION

In conclusion, we have demonstrated exchange control, which forms the basis for two-qubit gates between spin qubits, in an MOS DQD device fabricated using a 300 mm wafer process on natural silicon. The quality of the manufacturing manifests in the low detuning noise and relatively long T_2^* for a natural silicon MOS device. These results highlight the advantages of industrial manufacturing and encourage follow-up studies in isotopically enriched Si samples, which, during the review of our manuscript, have now been conducted in Ref. [66]. Additionally, similar to previous work [13, 21], adapting dedicated gates to primarily control exchange strength over a wider range could (i) enable symmetric exchange pulses and (ii) reduce $J/\Delta E_z$ well below 1, which should lead to an overall reduction in sensitivity to charge noise.

Furthermore, we have expanded the portfolio of disper-

sive readout methods by introducing the radio-frequency electron cascade, which, with its enhanced gain, demonstrates the highest performance for dispersive readout in planar MOS devices. Regarding scalability, the radio-frequency driven electron cascade can be extended to larger arrays for distant readout, eliminating the need for swap-based schemes that rely on shuttling information to a sensor [67]. As shown in Fig. 6, this extension builds upon existing schemes for two-dimensional grids using data and ancilla qubits [4, 15]. In this schematic, we assume that the tunnel barriers between each QD can be precisely controlled, enabling optimal readout fidelity through tuning t_c [51]. Figure 6(a) illustrates the readout protocol in a simplified one-dimensional array. In order to readout the data qubit Q_D at the periphery of the unit cell, the data qubit is tunnel-coupled to a neighbouring ancilla qubit Q_A . The ancilla qubit, in turn, is capacitively coupled to a chain of DQDs configured in the cascade configuration, eventually connected to a reservoir. An rf-drive applied to the ancilla-data DQD initiates the cascade, propagating along the chain to a readout reservoir. This scheme uniquely enables the simultaneous readout of distant data qubits through frequency multiplexing at the readout tank circuit. In contrast to previous work [44], by driving multiple cascade chains at distinct frequencies, multiple distant qubits can be readout simultaneously, as shown in Fig. 6(b). Furthermore, the combination of unit cells into a dense, scalable 2D grid allows readout resource sharing, resulting in the system being resilient to failure points such as faulty QDs or reservoirs, as demonstrated in Fig. 6(c).

METHODS

Fabrication details. The device measured in this study consists of three 30 nm-thick in-situ n^+ phosphorus-doped polycrystalline silicon gate layers formed with a wafer-level electron-beam patterning process [35, 36]. We use a high-resistivity (>3 k Ω /cm) p -type Si wafer. First, a 8 nm-thick, high quality SiO_2 layer is grown thermally to minimize the density of defects in the oxide and at the interface. Then, we subsequently pattern the gate layers using litho-etch processes and electrically isolate them from one another with a 5 nm-thick blocking high-temperature deposited SiO_2 [36]. We employ the first layer of gates (closest to the silicon substrate) to provide in-plane lateral confinement in the direction perpendicular to the double quantum dot axis. We use the second layer of gates (G_2 in this case) to form and control primarily quantum dot, Q_2 . Finally, we use the third gate layer to form and control quantum dot, Q_1 , via G_1 and both the multi-electron quantum dot, Q_{ME} , and reservoir via G_S , as shown in Fig. 1(a).

Measurement set-up. We perform the measurements at the base temperature of a dilution refrigerator ($T \sim 10$ mK). We send low-frequency signals through cryogenic low-pass filters with a cut-off frequency of

65 kHz, while we apply pulsed signals through attenuated coaxial lines. Both signals are combined through bias-Ts at the sample PCB (printed circuit-board) level. The PCB was made from RO4003C 0.8 mm thick with an immersion silver finish. For readout, we use radio-frequency reflectometry applied on the ohmic contact of the device. We send radio-frequency signals through attenuated coaxial lines to an on-PCB LC resonator, arranged in a parallel configuration, formed by a coupling capacitor (C_c), a 100 nm-thick NbTi superconducting spiral inductor (L) and the parasitic capacitance to ground (C_p), as shown in Fig. 1(b). We drive the resonator at 512.25 MHz which is the frequency of the system when G_S is well above threshold. The reflected rf signal is then amplified at 4K and room temperature, followed by quadrature demodulation, from which the amplitude and phase of the reflected signal were obtained (homodyne detection).

Radio-frequency cascade readout performance. The SNR of the interdot charge transition shown in Fig. 2(b) is determined by fitting the signal to an expression proportional to the quantum capacitance $\propto \partial^2 E / \partial \epsilon^2$ [40, 42],

$$V_{I,Q} \propto V_{I,Q}^0 - S_{I,Q} \frac{(2t_c)^3}{((\epsilon - \epsilon_0)^2 + (2t_c)^2)^{\frac{3}{2}}}, \quad (4)$$

where t_c is the tunnel coupling, ϵ_0 is the detuning value of the centre of the peak, and $S_{I,Q}$ and $V_{I,Q}^0$ are the voltage signal and voltage offset in phase and quadrature components of the measured rf-response, respectively. The power SNR is determined by combining the measured in-phase and quadrature voltage signal components of the reflected radio-frequency signal,

$$\text{SNR} = \frac{S_I^2 + S_Q^2}{0.5(\sigma_I^2 + \sigma_Q^2)} \quad (5)$$

where $S_{\text{rf},I(Q)}$ and $\sigma_{\text{rf},I(Q)}$ are indicated in Fig. 2(b), representing the signal and the standard deviation in background signal (away from zero detuning), respectively. Here, we assume a white noise spectrum dominated by the first cryogenic amplification stage [68]. In the measurements acquired throughout the text, the applied rf-power is $P_{\text{rf}} = -88.5$ dBm, corresponding to a power $\text{SNR} = (3.4 \pm 0.1) \times 10^3$. The minimum integration time is determined using [40],

$$\tau_{\text{min}} = \frac{N_{\text{avg}}}{2\Delta f \text{ SNR}} \quad (6)$$

where $N_{\text{avg}} = 4000$ is the number of averages used in the measurement, and $\Delta f = 1.53 f_{\text{LPF}}$ is the measurement bandwidth set by the low-pass filter cutoff frequency $f_{\text{LPF}} = 100$ kHz. Together, these two parameters give the noise equivalent integration time $\tau_{\text{NE}} = 13$ ms for the measurement in Fig. 2(b). Substituting the SNR into Eq. (6) we find a minimum integration time $\tau_{\text{min}} = 7.6 \pm 0.2$ μ s. In combination with the relaxation

time T_1 extracted in Fig. 2(e), the readout fidelity can be calculated using the following expression [37],

$$\mathcal{F}_r = \frac{1}{2} \left[1 + \operatorname{erf} \left(\sqrt{\frac{\tau_{\text{int}}}{8\tau_{\text{min}}}} \right) \exp \left(-\frac{\tau_{\text{int}}}{2T_1} \right) \right] \quad (7)$$

where τ_{int} is the integration time and $\operatorname{erf}(x)$ is the Gauss error function. The corresponding readout infidelity $1 - \mathcal{F}_r$ is shown in Fig. 2(f).

We define the detuning fluctuations associated with the rf excitation to be given by [40],

$$\delta\epsilon_{\text{rms}}^{\text{rf}} = \frac{\alpha_{21} V_{\text{dev}}}{\sqrt{2}}, \quad (8)$$

where $\alpha_{21} = \alpha_{\text{R},2} - \alpha_{\text{R},1}$ and V_{dev} is the voltage excitation at the reservoir ohmic contact, from input rf signal V_{in} [69],

$$V_{\text{dev}} = \frac{2C_C Q_L V_{\text{in}}}{C_C + C_P} \quad (9)$$

where $Q_L = 100$ is the loaded quality factor of the resonator depicted in Fig. 1(b), and rms $V_{\text{in}} = 8.4 \mu\text{V}$ corresponding to input $P_{\text{rf}} = -88.5 \text{ dBm}$. We then estimate an upper bound to $\alpha_{21} \geq 0.01$ by re-arranging Eq. (1), assuming $\alpha_{\text{R},\text{ME}} = 0.35 \pm 0.15$. The resulting rf-induced fluctuation in detuning is then, $\delta\epsilon_{\text{rms}}^{\text{rf}} \leq 2.7 \pm 0.6 \mu\text{eV}$.

Control sequence and charge noise estimation.

The pulse sequence implemented to demonstrate exchange control is as follows:

1. E: Empty quantum dot Q_1 by biasing the gate voltages such that the ground state is in the (0,1) charge configuration, over a duration of 100 ns.
2. E-I: Initialise the ground state $|S\rangle$ via an adiabatic ramp from the (0,1) to (0,2) configuration, over a duration of 10 μs .
3. I-S: Non-adiabatic pulse across the $|S\rangle$ - $|T_-\rangle$ anti-crossing to $\epsilon = 0$, over a duration of 100 ns. Establishing a symmetric detuning point to apply subsequent ramps.
4. S-P: Adiabatic ramp with respect to ΔE_z to $\epsilon = 0.926 \text{ meV}$ over a duration of 250 ns. Initialising $|\downarrow\uparrow\rangle$ where $J < \Delta E_z$.
5. P-J-P: Non-adiabatic pulse to near zero detuning ϵ_J and back where $J \gg \Delta E_z$, for variable duration τ_J .
6. P-M: Reverse adiabatic ramp to $\epsilon = 0$, projecting the final state onto $|S\rangle$ or $|T_0\rangle$ for readout.
7. M: Pre-measure delay of 6 μs is waited over before integrating for a measurement time of 8 μs .

The total duty cycle of the control sequence, $T_{\text{rep}} \approx 25 \mu\text{s}$, provides the high frequency f_{high} bound we integrate over to estimate S_0 , the power spectral density noise at 1 Hz. In combination with the total time to

acquire a trace of exchange oscillations, $T_M = 1/f_{\text{low}} = 0.3 \text{ h}$, we can estimate S_0 from [70],

$$\delta\epsilon_{\text{rms}} = \sqrt{2 \int_{f_{\text{low}}}^{f_{\text{high}}} S_\epsilon(f) df} \quad (10)$$

where the power spectral density of charge noise has the functional form $S_\epsilon(f) = S_0/f^\alpha$ with typical values of α ranging from 1 to 2. Considering the measured integrated charge noise ($\delta\epsilon_{\text{rms}} = 5.4 \mu\text{eV}$), we estimate an upper and lower bound of $\sqrt{S_0^{\alpha=1}} = 0.91 \mu\text{eV}/\sqrt{\text{Hz}}$ and $\sqrt{S_0^{\alpha=2}} = 0.12 \mu\text{eV}/\sqrt{\text{Hz}}$ respectively. This result is on par with the state-of-the-art reported in planar MOS devices [35] and strained Ge wells (Ge/SiGe) [61] $\sqrt{S_0} = 0.6 \pm 0.3 \mu\text{eV}/\sqrt{\text{Hz}}$, as well as Si wells in Si/SiGe heterostructures $\sqrt{S_0} = 0.3 - 0.8 \mu\text{eV}/\sqrt{\text{Hz}}$ [56, 62].

SUPPLEMENTARY INFORMATION

S1. ELECTROSTATIC REQUIREMENTS FOR RF-DRIVEN ELECTRON CASCADE READOUT

The conditions for rf-driven electron cascade are similar to those stated in a previous report on electron cascade with a proximal charge sensor [44]. It can be understood by considering the electrochemical potentials μ_i for each quantum dot Q_i , as well as the given charge configuration $(N_{Q_1}, N_{Q_2}, N_{Q_{\text{ME}}})$ where N_{Q_i} refers to the number of charges in dot Q_i , as shown in Fig. 1 of the main text. For cascade to occur the DQD must be tuned to the $Q_1 - Q_2$ inter-dot charge transition, such that

$$\mu_{Q_1}(1, 1, N) = \mu_{Q_2}(0, 2, N - 1). \quad (11)$$

Note that the opposite inter-dot charge transition $\mu_{Q_1}(2, 0, N) = \mu_{Q_2}(1, 1, N)$ also satisfies this condition. In addition to this, the reservoir-adjacent dot (Q_{ME}) must be tuned such that

$$\mu_{Q_{\text{ME}}}(1, 1, N) < 0 < \mu_{Q_{\text{ME}}}(0, 2, N), \quad (12)$$

where the Fermi level of the reservoir is referenced to 0 and

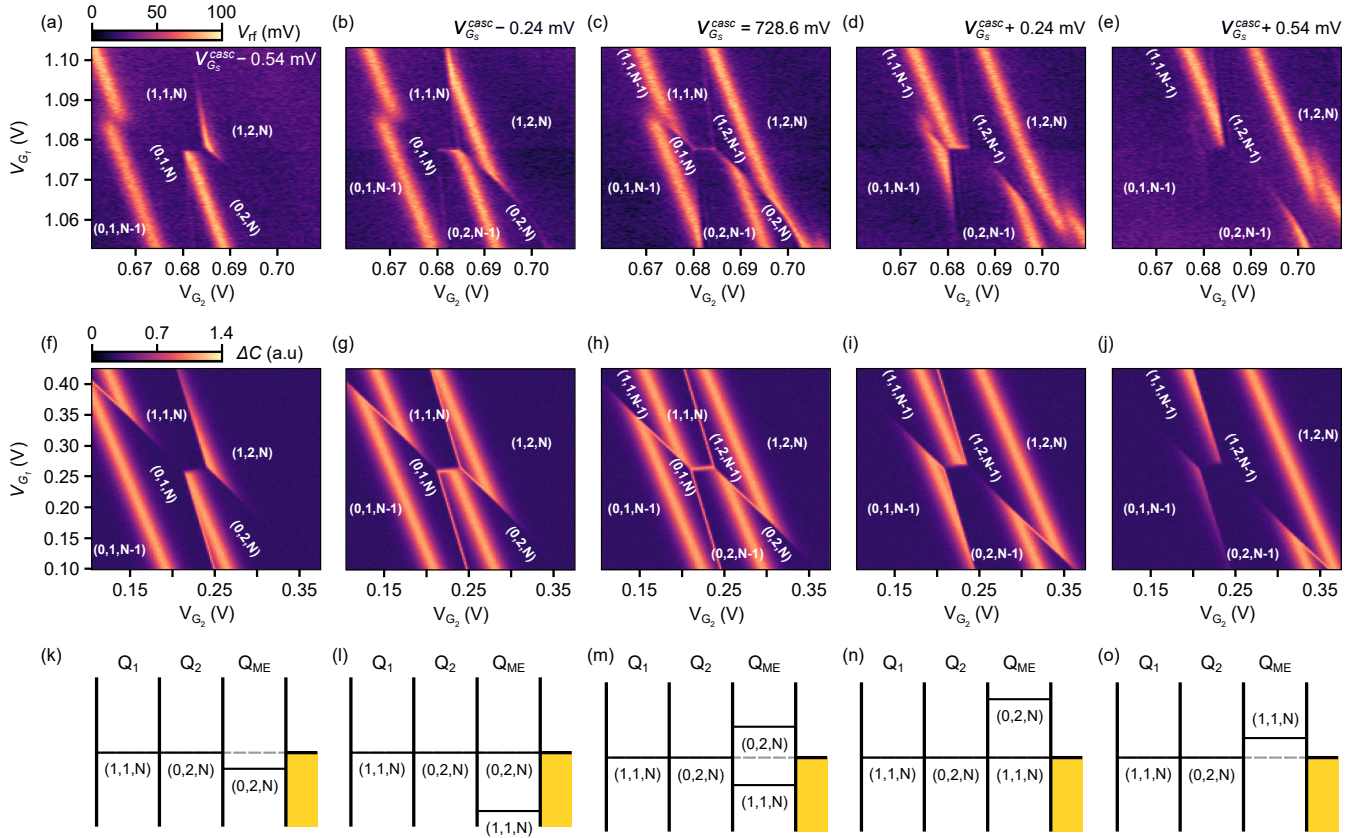
$$\Delta\mu_{Q_{\text{ME}}} = \mu_{Q_{\text{ME}}}(0, 2, N) - \mu_{Q_{\text{ME}}}(1, 1, N) \gg 3.5k_B T, \quad (13)$$

so the shift of the Q_{ME} Coulomb oscillation due to the interdot charge transition is much larger than the Fermi broadening of the reservoir. Here k_B is the Boltzmann constant and T the temperature.

The rf mode of the cascade drive introduces an additional condition that relates to the applied rf modulation amplitude V_{rf} ,

$$\Delta\mu_{Q_2-Q_1} < eV_{\text{rf}} \ll \Delta\mu_{Q_{\text{ME}}} \quad (14)$$

where $\Delta\mu_{Q_2-Q_1} = \mu_{Q_2}(1, 1, N) - \mu_{Q_1}(0, 2, N - 1)$. This ensures that the rf modulation only drives tunneling



Supplementary Fig. S1. | Tuning the radio-frequency driven electron cascade. **a-e**, Charge stability diagrams as a function of the DQD gate voltages $V_{G1} - V_{G2}$. The multi-electron QD bias V_{GS} is varied in each panel, defined with respect to V_{GS}^{casc} , the bias where the conditions for cascade are observed, shown in panel **c**. This is the bias utilized in the main text of the manuscript. **f-j**, Simulated charge stability diagrams using the methods described in Supplementary Section **S3**. **k-o** Schematic depiction of the electrochemical levels for the corresponding bias conditions, arranged column-wise.

events between Q_1 and Q_2 , without directly driving tunneling events between Q_{ME} and the reservoir.

Tuning the quantum dot array into rf-driven electron cascade requires precise control of the electrochemical potentials of the QDs, to the order of 10s of microvolts in the device presented here. The tuning procedure is most clearly demonstrated in the $V_{Q1} - V_{Q2}$ gate-voltage-space, as shown in Supplementary Fig. **S1** where in each panel V_{GS} is varied, bringing the system into and out of cascade. In this configuration, the range of V_{GS} bias voltages satisfying the conditions for cascade are given by $V_{GS}^{casc} = 728.6 \pm 0.1$ mV, a relatively narrow range of voltages as compared to the 14 mV addition voltage of Q_{ME} .

Supplementary Figure **S1** (a) and (e) shows two limiting cases, in which the $\mu_{Q_{ME}}(0, 2, N)$ or $\mu_{Q_{ME}}(1, 1, N)$ potentials do not meet the condition set by Eq. (12), i.e. the levels are below or above the Fermi level of the reservoir, respectively. Similar cases are observed in panels (b) and (d), where $\mu_{Q_{ME}}(0, 2, N)$ or $\mu_{Q_{ME}}(1, 1, N)$ now just align with the Fermi level in the reservoir but are within its Fermi broadening. In panel (b), the Q_{ME} transition is present in the $(0, 2, N-1) - (0, 2, N)$ occu-

pation regime, but absent in the $(1, 1, N-1) - (1, 1, N)$ regime. Likewise, in panel (d), the Q_{ME} transition is present in the $(1, 1, N-1) - (1, 1, N)$ regime but absent in the $(0, 2, N-1) - (0, 2, N)$ regime. The contrast in signal between the different charge occupations shown in Supplementary Fig. **S1**(b) and (d) is well-suited to standard charge sensing. It is only in panel (c), when the sequential tunneling event occurs, the cascade conditions are met and we observe the enhanced intensity of the interdot charge transition.

In panels (f-j), we present matching radio-frequency simulations of the triple QD system that highlight the enhanced intensity of the interdot charge transition (see Section. **S3**). Further, we supplement the explanation with schematics of the electrochemical levels in each V_{GS} conditions in panels (k-o).

S2. AMPLIFICATION FACTOR

Here, we obtain the expression for the signal amplification factor generated by the cascade process, i.e. Eq. (1) in the main text. To determine the amplification fac-

tor, we consider two different charge movement events as seen from the electrode connected to the resonator, in this case, the electron reservoir (R):

1. **In-situ dispersive readout** involving solely a charge transition between Q_1 and Q_2 .
2. **Cascade readout** involving (1) plus the cascaded charge transition between Q_{ME} and the reservoir.

To obtain the amplification factor, we first consider the expressions for the signal-to-noise ratio for case (1) [40]. In particular, we assume that the system is in the low frequency limit $\hbar f_{rf} \ll \Delta_c$ (where f_{rf} is the frequency of the resonator and $\Delta_c = 2t_c$), the small signal regime $Q_L \Delta C_Q / (2C_{tot}) \ll 1$ (where Q_L is the loaded quality factor of the resonator, ΔC_Q is the change in quantum capacitance of the system and C_{tot} the total capacitance of the system) and the large excitation regime, $\alpha_{21} e V_{dev} \gg \Delta_c$ to ensure an electron tunnels every half cycle of the rf excitation. Here $\alpha_{21} = \alpha_{R,2} - \alpha_{R,1}$ is the interdot lever arm as seen from the reservoir and V_{dev} is the amplitude of the oscillatory voltage arriving at the reservoir. In this case, the SNR is

$$SNR_{21} \propto \frac{(\alpha_{21}e)^2}{k_B T_n} Q_0 Z_r f_{rf}^2 = \frac{I_{R,21}^2 R}{k_B T_n}, \quad (15)$$

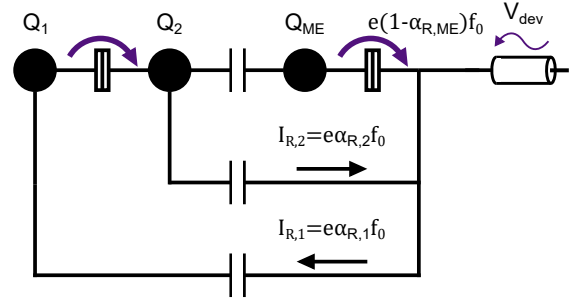
where T_n is the noise temperature of the system, $Q_0 = R\sqrt{C_p/L}$ is the internal quality factor of the resonator, $Z_r = \sqrt{L/C_p}$ is the resonator impedance, R is the resistance (in parallel with L and C_p) representing the losses in the resonator, and $I_{R,21}$ is the AC current amplitude produced at the reservoir by the oscillatory charge motion between Q_1 and Q_2 . Note that $\alpha_{21} e f_{rf} = I_{R,21}$ is the induced current at the reservoir due to the cyclic interdot tunneling.

We now perform the same calculation for the charge transition between the multi-electron quantum dot Q_{ME} and the reservoir R , a dot-to-reservoir transition [4]. Again, considering the small signal regime, the large excitation regime, $\alpha_{R,ME} e V_{dev} \gg k_B T$ (where $\alpha_{R,ME}$ is the lever arm from the reservoir to Q_{ME} and T is the electron temperature) and considering additionally the fast tunneling regime $\gamma \gg f_{rf}$ (where γ is the tunnel rate between Q_{ME} and R), we obtain

$$SNR_{ME} \propto \frac{(1 - \alpha_{ME})^2 e^2}{k_B T_n} Q_0 Z_r f_{rf}^2 = \frac{I_{R,ME}^2 R}{k_B T_n}. \quad (16)$$

Here, the resonator is coupled to Q_{ME} via a tunnel barrier, rather than a capacitively coupled gate, and hence the induced charge is $(1 - \alpha_{r,ME})e$.

After this analysis, we highlight a critical result: the SNR is proportional to the square of the AC current amplitude produced by the relevant process, whereas the other two parameters, R and T_n , are independent of the charge transfer process, particularly in the typical regime where the noise temperature is determined by the first amplifying stage.



Supplementary Fig. S2. | Schematic circuit depicting alternating current induced by the radio-frequency driven electron cascade. Two tunneling processes are depicted between tunnel coupled (1) quantum dots Q_1 and Q_2 and (2) Q_{ME} and the reservoir. The induced alternating current at the reservoir from each of these tunneling events is given by $I_{R,i} = e\alpha_{R,i}f_0$ where $i = 1, 2, ME$ and $\alpha_{R,i}$ are the corresponding lever arms, with rf drive frequency f_0 . The rf modulation applied to the system is represented by V_{dev} , the device voltage.

From this we can determine an expression for the amplification factor by considering the two tunneling processes presented in Supplementary Fig. S2. In process (1) the alternating current generated by cyclical tunneling from Q_1 to Q_2 is,

$$I_{R,21} = \alpha_{21} e f_{rf} = (\alpha_{r,2} - \alpha_{r,1}) e f_{rf}. \quad (17)$$

In process (2), in addition to the current produced by process (1), we have the current produced by the cascade process adding to a total of,

$$I_{\text{cascade}} \approx I_{R,21} + I_{R,ME} = (\alpha_{r,2} - \alpha_{r,1}) e f_{rf} + (1 - \alpha_{r,ME}) e f_{rf}. \quad (18)$$

The amplification factor A is then given by the ratio between the two processes,

$$A = \frac{I_{\text{cascade}}}{I_{R,21}} = 1 + \frac{1 - \alpha_{r,ME}}{\alpha_{r,2} - \alpha_{r,1}}. \quad (19)$$

S3. CHARGE STABILITY DIAGRAM SIMULATION

To simulate the cascade phenomena we observe in the main text, we calculate the charge stability diagram for a specific voltage configuration using the Constant Interaction Model [71]. The energies in this model are defined as

$$E = \frac{1}{2} \vec{V}^T \mathbf{C}_{cc}^{-1} \vec{V} \quad (20)$$

where \mathbf{C}_{cc} is the capacitance matrix for the QDs, containing the mutual capacitance between each pair

$$\mathbf{C}_{cc} = \begin{pmatrix} 35.000 & -4.882 & -1.886 \\ -4.882 & 27.936 & -0.402 \\ -1.886 & -0.402 & 42.048 \end{pmatrix} \quad (21)$$

where each element is given in aF and $\vec{V} = e(\mathbf{C}_{\text{cv}}\vec{V}_G - |e|\vec{N})$. Additionally we define \mathbf{C}_{cv} to represent the capacitance matrix governing the interactions between the gate and charges, containing the capacitance between each QD and the corresponding gates,

$$C_{\text{cv}} = \begin{pmatrix} 0.898 & 0.146 & 0.000 \\ 0.537 & 0.453 & 0.000 \\ 0.063 & 0.020 & 2.016 \end{pmatrix} \quad (22)$$

where each element is given in aF. The number of charges on each dot are given by \vec{N} , and \vec{V}_G denotes the applied gate voltages. Throughout the simulations, we use natural units and set the charge of the electron $e = 1$. We note that the ratio between capacitances in the matrices defined here are found to be in qualitative agreement with the data in Supplementary Fig. S1(a-e), however the magnitude of these capacitances have not been verified experimentally.

Without loss of generality, we assume that an M -quantum dot array can exist in a state from a set of L Fock states, denoted as $\mathcal{F} = \{\Lambda_j = (\lambda_{1,j}, \dots, \lambda_{M,j}) \mid \lambda_{i,j} \in \mathbb{Z}^+, \forall j = 1, 2, \dots, L\}$. Here $\lambda_{i,j}$ represents the occupancy number of quantum dot i in Fock state Λ_j .

In radio-frequency reflectometry, the measured signal is directly proportional to the change in capacitance of the system, this can be described mathematically as

$$\Delta C_j = \frac{dQ_T}{dV_j}, \quad (23)$$

here Q_T denotes the total charge of the system and V_j represents the j^{th} gate. We take inspiration from [72] and rewrite the change in capacitance as measured from gate V_j to be

$$\Delta C_j = \sum_{i=1}^M C_{i,j} = e \sum_{i=1}^M \alpha_{i,j} \frac{d\langle n_i \rangle}{dV_j}. \quad (24)$$

In this context, $C_{i,j}$ represents the capacitance felt from dot i by gate j . The average occupancy of dot i is denoted $\langle n_i \rangle$. The lever arm matrix is defined as $\alpha = \mathbf{C}_{\text{cc}}^{-1} \mathbf{C}_{\text{cv}}$, which links gate-induced potential changes to the charge states of the quantum dots. To calculate $\langle n_i \rangle$, we iterate through each Fock state in \mathcal{F} and compute its corresponding probability. Subsequently, a weighted sum of the occupation numbers of each Fock state at position i is performed, expressed as

$$\langle n_i \rangle = \sum_{k=1}^L \lambda_{i,k} \cdot P_k, \quad (25)$$

where P_k represents the probability of the quantum dot array being in the Fock state Λ_k . We assume a Boltzmann distribution and write the probability accordingly;

$$P_k = \frac{1}{Z} \exp\left(-\frac{\epsilon_k}{k_b T}\right) = \frac{\exp\left(-\frac{\epsilon_k}{k_b T}\right)}{\sum_{l=1}^L \exp\left(-\frac{\epsilon_l}{k_b T}\right)} \quad (26)$$

where Z represents the partition function, and ϵ_k represents the energy required for quantum dot array to be in the Fock state Λ_k . Substituting this into equation (25), we obtain;

$$\langle n_i \rangle = \sum_{k=1}^L \lambda_{i,k} \cdot \frac{\exp\left(-\frac{\epsilon_k}{k_b T}\right)}{\sum_{l=1}^L \exp\left(-\frac{\epsilon_l}{k_b T}\right)} \quad (27)$$

This term can be further substituted into equation (24), to obtain;

$$\begin{aligned} \Delta C_{j,\text{tot}} &= \sum_{i=1}^M C_{i,j} \\ &= e \sum_i \alpha_{i,j} \frac{d}{dV_j} \left(\sum_{k=1}^L \lambda_{i,k} \cdot \frac{\exp\left(-\frac{\epsilon_k}{k_b T}\right)}{\sum_{l=1}^L \exp\left(-\frac{\epsilon_l}{k_b T}\right)} \right) \end{aligned} \quad (28)$$

We use the above formalism to simulate the charge stability diagrams in the $V_{G_1} - V_{G_2}$ gate-voltage space. This can be seen in Supplementary Fig. S1(f-j), where different voltage configurations were applied to the multi-electron dot via V_{G_S} .

S4. MAGNETOSPECTROSCOPY SIMULATION

Here, we describe the simulations of the magnetospectroscopy map in the inset of Fig. 1(c) in the main text. that allow us to estimate both the tunnel coupling t_c and the electron temperature T_e . We utilize the simplified Hamiltonian:

$$H = \frac{1}{2} \begin{pmatrix} \varepsilon & \Delta_c & 0 & 0 & 0 \\ \Delta_c & -\varepsilon & 0 & 0 & 0 \\ 0 & 0 & -\varepsilon - \hat{B} & 0 & 0 \\ 0 & 0 & 0 & -\varepsilon & 0 \\ 0 & 0 & 0 & 0 & -\varepsilon + \hat{B} \end{pmatrix}, \quad (30)$$

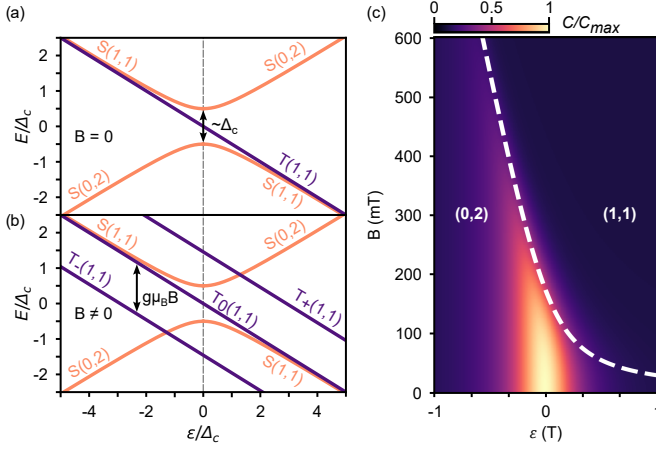
where $\hat{B} = 2g\mu_B B$, g is the electron g-factor (which we approximate to 2 for both QDs). Then, we calculate the quantum capacitance of the system, C_Q , given by,

$$C_Q = - \sum_i (e\alpha)^2 \frac{\partial^2 E_i}{\partial \varepsilon^2} P_i^{\text{th}}. \quad (31)$$

where E_i are the eigenenergies of the above Hamiltonian and P_i^{th} is the thermal probability of the state i ,

$$P_i^{\text{th}} = \exp(-E_i/k_B T_e)/Z. \quad (32)$$

Here, T_e is the DQD temperature and Z is the partition function over all states [73]. We plot the results of the simulations in Supplementary Fig. S3 where, in panel (a) and (b), we show the energy spectrum of the system as a function of detuning for $B = 0.5$ T and 0 T, respectively, and in panel (c), we plot the normalised quantum capacitance of the systems as a function of ε and B . We find that the best match between the data and simulations occurs when $t_c = 2.4$ GHz and $T_e = 50$ mK.



Supplementary Fig. S3. | Magneto-spectroscopy simulation of the (0,2)-(1,1) inter-dot charge transition. Eigenenergies of the two-electron spin states, singlet $|S\rangle$ and triplet $|T\rangle$ states as a function of detuning ε normalised by tunnel coupling $\Delta = 2t_c$. For **a**, applied magnetic field $B = 0$ mT and **b** $B = 500$ mT. **c** Normalised quantum capacitance simulation versus detuning and magnetic field, with the degeneracy point of the $|S\rangle$ - $|T_-\rangle$ crossing overlaid (white dashed line).

DATA AVAILABILITY

The data that support the plots within this paper and other findings of this study are available from the corresponding authors upon reasonable request.

ACKNOWLEDGEMENTS

We acknowledge helpful conversations with H. Jnane, A. Seigel, S.C. Benjamin, A.J. Fisher and G. Burkard at Quantum Motion. We also acknowledge technical support from G. Antilen Jacob at the Lon-

don Centre for Nanotechnology. This work received support from the European Union's Horizon 2020 research and innovation programme under grant agreement No. 951852 (Quantum Large Scale Integration in Silicon); from the Engineering and Physical Sciences Research Council (EPSRC) under grant Nos. (EP/S021582/1), (EP/L015978/1), (EP/T001062/1) and (EP/L015242/1); and from Innovate UK under grant Nos. (43942) and (10015036). T.M. acknowledges support from the Winton Programme for the Physics of Sustainability. M.F.G.Z. acknowledges support from the UKRI Future Leaders Fellowship (MR/V023284/1).

AUTHOR CONTRIBUTIONS

J.F.C.W. conducted the experiments and analysed the results presented in this work with input from R.C.C.L., M.A.F., M.F.G.Z. and J.J.L.M.; J.F.C.W., M.A.F. and R.C.C.L. conducted preliminary experiments; T.M. and G.A.O. developed the quantum dot rf simulator in Supplementary Section 4 informed by electrostatic modelling from J.W.; T. M. performed and wrote about the simulations under the supervision of D. F. W. and M. F. G. Z.; S.M.P. designed the device under the supervision of M.A.F., M.F.G.Z. and J.J.L.M.; J.J. and S.K. fabricated the device under the supervision of B.G.; F.E.v.H. characterised the superconducting resonator under the supervision of M.F.G.Z.; N.J. maintained the experimental setup; J.F.C.W., M.F.G.Z. and J.J.L.M. wrote the manuscript with input from R.C.C.L., M.A.F., N.J. and S.M.P.; M.F.G.Z. and J.J.L.M. conceived and oversaw the experiment.

COMPETING INTERESTS

Quantum Motion Technologies Limited has filed a patent application related to this work: EP23206749.6 (Europe) by J.F.C.W., R.C.C.L., M.A.F. and M.F.G.Z.

-
- [1] J. Yoneda, K. Takeda, A. Noiri, T. Nakajima, S. Li, J. Kamioka, T. Kodera, and S. Tarucha, Quantum non-demolition readout of an electron spin in silicon, *Nat. Commun* **11**, 1144 (2020).
 - [2] K. Takeda, A. Noiri, T. Nakajima, T. Kobayashi, and S. Tarucha, Quantum error correction with silicon spin qubits, *Nature* **608**, 682 (2022).
 - [3] E. J. Connors, J. Nelson, and J. M. Nichol, Rapid high-fidelity spin-state readout in Si/Si-Ge quantum dots via rf reflectometry, *Phys. Rev. Appl.* **13**, 024019 (2020).
 - [4] G. A. Oakes, V. N. Ciriano-Tejel, D. F. Wise, M. A. Fogarty, T. Lundberg, C. Lainé, S. Schaal, F. Martins, D. J. Ibberson, L. Hutin, B. Bertrand, N. Stelmashenko, J. W. A. Robinson, L. Ibberson, A. Hashim, I. Siddiqi, A. Lee, M. Vinet, C. G. Smith, J. J. L. Morton, and M. F. Gonzalez-Zalba, Electron cascade for distant spin readout, *Phys. Rev. X* **13**, 011023 (2023).
 - [5] K. Takeda, A. Noiri, T. Nakajima, L. C. Camenzind, T. Kobayashi, A. Sammak, G. Scappucci, and S. Tarucha, Rapid single-shot parity spin readout in a silicon double quantum dot with fidelity exceeding 99%, *npj Quantum Information* **10**, 22 (2024).
 - [6] L. C. Camenzind, S. Geyer, A. Fuhrer, R. J. Warburton, D. M. Zumbühl, and A. V. Kuhlmann, A hole spin qubit in a fin field-effect transistor above 4 kelvin, *Nature Electronics* **5**, 178 (2022).
 - [7] J. Yoneda, K. Takeda, T. Otsuka, T. Nakajima, M. R. Delbecq, G. Allison, T. Honda, T. Kodera, S. Oda, Y. Hoshi, N. Usami, K. M. Itoh, and S. Tarucha, A quantum-dot spin qubit with coherence limited by charge noise and fidelity higher than 99.9%, *Nature Nanotech-*

- nology **13**, 102 (2018).
- [8] C. H. Yang, K. W. Chan, R. Harper, W. Huang, T. Evans, J. C. C. Hwang, B. Hensen, A. Laucht, T. Tanttu, F. E. Hudson, S. T. Flammia, K. M. Itoh, A. Morello, S. D. Bartlett, and A. S. Dzurak, Silicon qubit fidelities approaching incoherent noise limits via pulse engineering, *Nature Electronics* **2**, 151 (2019).
 - [9] X. Xue, M. Russ, N. Samkharadze, B. Undseth, A. Sammak, G. Scappucci, and L. M. K. Vandersypen, Quantum logic with spin qubits crossing the surface code threshold, *Nature* **601**, 343 (2022).
 - [10] M. T. Mądzik, S. Asaad, A. Youssry, B. Joecker, K. M. Rudinger, E. Nielsen, K. C. Young, T. J. Proctor, A. D. Baczewski, A. Laucht, V. Schmitt, F. E. Hudson, K. M. Itoh, A. M. Jakob, B. C. Johnson, D. N. Jamieson, A. S. Dzurak, C. Ferrie, R. Blume-Kohout, and A. Morello, Precision tomography of a three-qubit donor quantum processor in silicon, *Nature* **601**, 348 (2022).
 - [11] A. Noiri, K. Takeda, T. Nakajima, T. Kobayashi, A. Sammak, G. Scappucci, and S. Tarucha, Fast universal quantum gate above the fault-tolerance threshold in silicon, *Nature* **601**, 338 (2022).
 - [12] A. R. Mills, C. R. Guinn, M. J. Gullans, A. J. Sigillito, M. M. Feldman, E. Nielsen, and J. R. Petta, Two-qubit silicon quantum processor with operation fidelity exceeding 99%, *Science Advances* **8**, eabn5130 (2022).
 - [13] T. Tanttu, W. H. Lim, J. Y. Huang, N. Dumoulin Stuyck, W. Gilbert, R. Y. Su, M. Feng, J. D. Cifuentes, A. E. Seedhouse, S. K. Seritan, C. I. Ostrove, K. M. Rudinger, R. C. C. Leon, W. Huang, C. C. Escott, K. M. Itoh, N. V. Abrosimov, H.-J. Pohl, M. L. W. Thewalt, F. E. Hudson, R. Blume-Kohout, S. D. Bartlett, A. Morello, A. Laucht, C. H. Yang, A. Saraiva, and A. S. Dzurak, Assessment of the errors of high-fidelity two-qubit gates in silicon quantum dots, *Nat. Phys.* [10.1038/s41567-024-02614-w](https://doi.org/10.1038/s41567-024-02614-w) (2024).
 - [14] L. Kranz, S. Roche, S. K. Gorman, J. G. Keizer, and M. Y. Simmons, High-fidelity cnot gate for donor electron spin qubits in silicon, *Phys. Rev. Appl.* **19**, 024068 (2023).
 - [15] A. G. Fowler, M. Mariantoni, J. M. Martinis, and A. N. Cleland, Surface codes: Towards practical large-scale quantum computation, *Phys. Rev. A* **86**, 032324 (2012).
 - [16] S. G. J. Philips, M. T. Mądzik, S. V. Amitonov, S. L. de Snoo, M. Russ, N. Kalhor, C. Volk, W. I. L. Lawrie, D. Brousse, L. Tryputen, B. P. Wuetz, A. Sammak, M. Veldhorst, G. Scappucci, and L. M. K. Vandersypen, Universal control of a six-qubit quantum processor in silicon, *Nature* **609**, 919 (2022).
 - [17] M. F. Gonzalez-Zalba, S. de Franceschi, E. Charbon, T. Meunier, M. Vinet, and A. S. Dzurak, Scaling silicon-based quantum computing using cmos technology, *Nature Electronics* **4**, 872 (2021).
 - [18] S. J. Pauka, K. Das, R. Kalra, A. Moini, Y. Yang, M. Trainer, A. Bousquet, C. Cantaloube, N. Dick, G. C. Gardner, M. J. Manfra, and D. J. Reilly, A cryogenic cmos chip for generating control signals for multiple qubits, *Nat Electron* **4**, 64 (2021).
 - [19] A. Ruffino, T.-Y. Yang, J. Michniewicz, Y. Peng, E. Charbon, and M. F. Gonzalez-Zalba, A cryo-cmos chip that integrates silicon quantum dots and multiplexed dispersive readout electronics, *Nat Electron* **5**, 53 (2022).
 - [20] M. Veldhorst, C. H. Yang, J. C. C. Hwang, W. Huang, J. P. Dehollain, J. T. Muhonen, S. Simmons, A. Laucht, F. E. Hudson, K. M. Itoh, A. Morello, and A. S. Dzurak, A two-qubit logic gate in silicon, *Nature* **526**, 410 (2015).
 - [21] C. H. Yang, R. C. Leon, J. C. Hwang, A. Saraiva, T. Tanttu, W. Huang, J. C. Lemyre, K. W. Chan, K. Y. Tan, F. E. Hudson, K. M. Itoh, A. Morello, M. Pioro-Ladrière, A. Laucht, and A. S. Dzurak, Operation of a silicon quantum processor unit cell above one kelvin, *Nature* **580**, 350 (2020).
 - [22] B. M. Maune, M. G. Borselli, B. Huang, T. D. Ladd, P. W. Deelman, K. S. Holabird, A. A. Kiselev, I. Alvarado-Rodriguez, R. S. Ross, A. E. Schmitz, M. Sokolich, C. A. Watson, M. F. Gyure, and A. T. Hunter, Coherent singlet-triplet oscillations in a silicon-based double quantum dot, *Nature* **481**, 344 (2012).
 - [23] E. Kawakami, P. Scarlino, D. R. Ward, F. R. Braakman, D. E. Savage, M. G. Lagally, M. Friesen, S. N. Coppersmith, M. A. Eriksson, and L. M. K. Vandersypen, Electrical control of a long-lived spin qubit in a si/sige quantum dot, *Nat. Nanotechnol.* **9**, 666 (2014).
 - [24] H. C. George, M. T. Mądzik, E. M. Henry, A. J. Wagner, M. M. Islam, F. Borjans, E. J. Connors, J. Corrigan, M. Curry, M. K. Harper, D. Keith, L. Lampert, F. Luthi, F. A. Mohiyaddin, S. Murcia, R. Nair, R. Nahm, A. Nethewala, S. Neyens, B. Patra, R. D. Rahrarjo, C. Rogan, R. Savvitsky, T. F. Watson, J. Ziegler, O. K. Zietz, S. Pellerano, R. Pillarisetty, N. C. Bishop, S. A. Bojarski, J. Roberts, and J. S. Clarke, 12-spin-qubit arrays fabricated on a 300 mm semiconductor manufacturing line, *Nano Letters* **25**, 793 (2025).
 - [25] M. A. Fogarty, K. W. Chan, B. Hensen, W. Huang, T. Tanttu, C. H. Yang, A. Laucht, M. Veldhorst, F. E. Hudson, K. M. Itoh, D. Culcer, T. D. Ladd, A. Morello, and A. S. Dzurak, Integrated silicon qubit platform with single-spin addressability, exchange control and single-shot singlet-triplet readout, *Nat. Commun* **9**, 4370 (2018).
 - [26] R. M. Jock, N. T. Jacobson, P. Harvey-Collard, A. M. Mounce, V. Srinivasa, D. R. Ward, J. Anderson, R. Manginell, J. R. Wendt, M. Rudolph, T. Pluym, J. K. Gamble, A. D. Baczewski, W. M. Witzel, and M. S. Carroll, A silicon metal-oxide-semiconductor electron spin-orbit qubit, *Nat. Commun* **9**, 1768 (2018).
 - [27] R. M. Jock, N. T. Jacobson, M. Rudolph, D. R. Ward, M. S. Carroll, and D. R. Luhman, A silicon singlet-triplet qubit driven by spin-valley coupling, *Nat. Commun* **13**, 641 (2022).
 - [28] R. Maurand, X. Jehl, D. Kotekar-Patil, A. Corna, H. Bohuslavskiy, L. Laviéville, L. Hutin, S. Barraud, M. Vinet, M. Sanquer, and S. D. Franceschi, A CMOS silicon spin qubit, *Nat. Commun* **7**, 13575 (2016).
 - [29] N. Piot, B. Brun, V. Schmitt, S. Zihlmann, V. P. Michal, A. Apra, J. C. Abadillo-Uriel, X. Jehl, B. Bertrand, H. Niebojewski, L. Hutin, M. Vinet, M. Urdampilleta, T. Meunier, Y.-M. Niquet, R. Maurand, and S. D. Franceschi, A single hole spin with enhanced coherence in natural silicon, *Nat. Nanotechnol.* **17**, 1072 (2022).
 - [30] A. M. J. Zwerver, T. Krähenmann, T. F. Watson, L. Lampert, H. C. George, R. Pillarisetty, S. A. Bojarski, P. Amin, S. V. Amitonov, J. M. Boter, R. Caudillo, D. Correias-Serrano, J. P. Dehollain, G. Droulers, E. M. Henry, R. Kotlyar, M. Lodari, F. Lüthi, D. J. Michalak, B. K. Mueller, S. Neyens, J. Roberts, N. Samkharadze, G. Zheng, O. K. Zietz, G. Scappucci, M. Veldhorst,

- L. M. K. Vandersypen, and J. S. Clarke, Qubits made by advanced semiconductor manufacturing, *Nat. Electron* **5**, 184 (2022).
- [31] R. Li, L. Petit, D. P. Franke, J. P. Dehollain, J. Helsen, M. Steudtner, N. K. Thomas, Z. R. Yoscovits, K. J. Singh, S. Wehner, L. M. K. Vandersypen, J. S. Clarke, and M. Veldhorst, A crossbar network for silicon quantum dot qubits, *Science Advances* **4**, eaar3960 (2018).
- [32] P. Pakkiam, A. V. Timofeev, M. G. House, M. R. Hogg, T. Kobayashi, M. Koch, S. Rogge, and M. Y. Simmons, Single-shot single-gate rf spin readout in silicon, *Phys. Rev. X* **8**, 041032 (2018).
- [33] A. West, B. Hensen, A. Jouan, T. Tanttu, C.-H. Yang, A. Rossi, M. F. Gonzalez-Zalba, F. Hudson, A. Morello, D. J. Reilly, and A. S. Dzurak, Gate-based single-shot readout of spins in silicon, *Nat. Nanotechnol.* **14**, 437 (2019).
- [34] G. Zheng, N. Samkharadze, M. L. Noordam, N. Kalhor, D. Brousse, A. Sammak, G. Scappucci, and L. M. K. Vandersypen, Rapid gate-based spin read-out in silicon using an on-chip resonator, *Nat. Nanotechnol.* **14**, 742 (2019).
- [35] A. Elsayed, M. Shehata, C. Godfrin, S. Kubicek, S. Massar, Y. Canvel, J. Jussot, G. Simion, M. Mongillo, D. Wan, B. Govoreanu, I. P. Radu, R. Li, P. V. Dorpe, and K. D. Greve, Low charge noise quantum dots with industrial cmos manufacturing, *npj Quantum Inf* **10**, 70 (2024).
- [36] N. I. D. Stuyck, R. Li, C. Godfrin, A. Elsayed, S. Kubicek, J. Jussot, B. T. Chan, F. A. Mohiyaddin, M. Shehata, G. Simion, Y. Canvel, L. Goux, M. Heyns, B. Govoreanu, and I. P. Radu, Uniform spin qubit devices with tunable coupling in an all-silicon 300 mm integrated process, in *2021 Symposium on VLSI Circuits* (2021) pp. 1–2.
- [37] J. Gambetta, W. A. Braff, A. Wallraff, S. M. Girvin, and R. J. Schoelkopf, Protocols for optimal readout of qubits using a continuous quantum nondemolition measurement, *Phys. Rev. A* **76**, 012325 (2007).
- [38] K. Ono, D. G. Austing, Y. Tokura, and S. Tarucha, Current rectification by pauli exclusion in a weakly coupled double quantum dot system, *Science* **297**, 1313 (2002).
- [39] J. M. Elzerman, R. Hanson, L. H. Willems van Beveren, B. Witkamp, L. M. K. Vandersypen, and L. P. Kouwenhoven, Single-shot read-out of an individual electron spin in a quantum dot, *Nature* **430**, 431 (2004).
- [40] F. Vigneau, F. Fedele, A. Chatterjee, D. Reilly, F. Kuemmeth, M. F. Gonzalez-Zalba, E. Laird, and N. Ares, Probing quantum devices with radio-frequency reflectometry, *Applied Physics Reviews* **10**, 021305 (2023).
- [41] R. J. Schoelkopf, P. Wahlgren, A. A. Kozhevnikov, P. Delsing, and D. E. Prober, The radio-frequency single-electron transistor (rf-set): A fast and ultrasensitive electrometer, *Science* **280**, 1238 (1998).
- [42] A. C. Betz, R. Wacquez, M. Vinet, X. Jehl, A. L. Saraiva, M. Sanquer, A. J. Ferguson, and M. F. Gonzalez-Zalba, Dispersively detected pauli spin-blockade in a silicon nanowire field-effect transistor, *Nano Lett* **15**, 4622 (2015).
- [43] P. Harvey-Collard, B. D’Anjou, M. Rudolph, N. T. Jacobson, J. Dominguez, G. A. Ten Eyck, J. R. Wendt, T. Pluym, M. P. Lilly, W. A. Coish, M. Pioro-Ladrière, and M. S. Carroll, High-fidelity single-shot readout for a spin qubit via an enhanced latching mechanism, *Phys. Rev. X* **8**, 021046 (2018).
- [44] C. J. van Diepen, T.-K. Hsiao, U. Mukhopadhyay, C. Reichl, W. Wegscheider, and L. M. K. Vandersypen, Electron cascade for distant spin readout, *Nat. Commun* **12**, 77 (2021).
- [45] M. Urdampilleta, D. J. Niegemann, E. Chanrion, B. Jadot, C. Spence, P.-A. Mortemousque, C. Bäuerle, L. Hutin, B. Bertrand, S. Barraud, R. Maurand, M. Sanquer, X. Jehl, S. De Franceschi, M. Vinet, and T. Meunier, Gate-based high fidelity spin readout in a cmos device, *Nat. Nanotechnol.* **14**, 737 (2019).
- [46] D. Gusenkova, M. Spiecker, R. Gebauer, M. Willsch, D. Willsch, F. Valenti, N. Karcher, L. Grünhaupt, I. Takmakov, P. Winkel, D. Rieger, A. V. Ustinov, N. Roch, W. Wernsdorfer, K. Michelsen, O. Sander, and I. M. Pop, Quantum nondemolition dispersive readout of a superconducting artificial atom using large photon numbers, *Phys. Rev. Appl.* **15**, 064030 (2021).
- [47] O. E. Dial, M. D. Shulman, S. P. Harvey, H. Bluhm, V. Umansky, and A. Yacoby, Charge noise spectroscopy using coherent exchange oscillations in a singlet-triplet qubit, *Phys. Rev. Lett.* **110**, 146804 (2013).
- [48] X. Wu, D. R. Ward, J. R. Prance, D. Kim, J. K. Gamble, R. T. Mohr, Z. Shi, D. E. Savage, M. G. Lagally, M. Friesen, S. N. Coppersmith, and M. A. Eriksson, Two-axis control of a singlet-triplet qubit with an integrated micromagnet, *Proc. Natl. Acad. Sci. U.S.A.* **111**, 11938 (2014).
- [49] D. J. Niegemann, V. El-Homsy, B. Jadot, M. Nurizzo, B. Cardoso-Paz, E. Chanrion, M. Dartiaillh, B. Klemm, V. Thiney, C. Bäuerle, P.-A. Mortemousque, B. Bertrand, H. Niebojewski, M. Vinet, F. Balestro, T. Meunier, and M. Urdampilleta, Parity and singlet-triplet high-fidelity readout in a silicon double quantum dot at 0.5 k, *PRX Quantum* **3**, 040335 (2022).
- [50] M. Hogg, P. Pakkiam, S. K. Gorman, A. V. Timofeev, Y. Chung, G. K. Gulati, M. G. House, and M. Y. Simmons, Single-shot readout of multiple donor electron spins with a gate-based sensor, *PRX Quantum* **4**, 010319 (2023).
- [51] C. Lainé, G. A. Oakes, V. Ciriano-Tejel, J. F. Chittcock-Wood, M. A. Fogarty, S. M. Patomäki, S. Kubicek, R. C. C. Leon, M. F. Gonzalez-Zalba, and J. J. L. Morton, High-fidelity dispersive spin sensing in a tuneable unit cell of silicon mos quantum dots, *In Preparation* (2025).
- [52] P. Apostolidis, B. J. Villis, J. F. Chittcock-Wood, J. M. Powell, A. Baumgartner, V. Vesterinen, S. Simbierowicz, J. Hassel, and M. R. Buitelaar, Quantum paraelectric varactors for radiofrequency measurements at millikelvin temperatures, *Nature Electronics* **7**, 760 (2024).
- [53] T. Nakajima, A. Noiri, J. Yoneda, M. R. Delbecq, P. Stano, T. Otsuka, K. Takeda, S. Amaha, G. Allison, K. Kawasaki, A. Ludwig, A. D. Wieck, D. Loss, and S. Tarucha, Quantum non-demolition measurement of an electron spin qubit, *Nat. Nanotechnol.* **14**, 555 (2019).
- [54] M. Veldhorst, R. Ruskov, C. H. Yang, J. C. C. Hwang, F. E. Hudson, M. E. Flatté, C. Tahan, K. M. Itoh, A. Morello, and A. S. Dzurak, Spin-orbit coupling and operation of multivalley spin qubits, *Phys. Rev. B* **92**, 201401 (2015).
- [55] T. Tanttu, B. Hensen, K. W. Chan, C. H. Yang, W. W. Huang, M. Fogarty, F. Hudson, K. Itoh, D. Culcer, A. Laucht, A. Morello, and A. Dzurak, Controlling spin-

- orbit interactions in silicon quantum dots using magnetic field direction, *Phys. Rev. X* **9**, 021028 (2019).
- [56] E. J. Connors, J. Nelson, L. F. Edge, and J. M. Nichol, Charge-noise spectroscopy of si/sige quantum dots via dynamically-decoupled exchange oscillations, *Nature Communications* **13**, 940 (2022).
- [57] S. D. Liles, D. J. Halverson, Z. Wang, A. Shamim, R. S. Eggli, I. K. Jin, J. Hillier, K. Kumar, I. Vorreiter, M. J. Rendell, J. Y. Huang, C. C. Escott, F. E. Hudson, W. H. Lim, D. Culcer, A. S. Dzurak, and A. R. Hamilton, A singlet-triplet hole-spin qubit in mos silicon, *Nat. Commun* **15**, 7690 (2024).
- [58] D. Jirovec, A. Hofmann, A. Ballabio, P. M. Mutter, G. Tavani, M. Botifoll, A. Crippa, J. Kukucka, O. Sagi, F. Martins, J. Saez-Mollejo, I. Prieto, M. Borovkov, J. Arbiol, D. Chrastina, G. Isella, and G. Katsaros, A singlet-triplet hole spin qubit in planar Ge, *Nat. Mater.* **20**, 1106 (2021).
- [59] J. D. Cifuentes, T. Tanttu, W. Gilbert, J. Y. Huang, E. Vahapoglu, R. C. C. Leon, S. Serrano, D. Otter, D. Dunmore, P. Y. Mai, F. Schlattner, M. Feng, K. Itoh, N. Abrosimov, H.-J. Pohl, M. Thewalt, A. Laucht, C. H. Yang, C. C. Escott, W. H. Lim, F. E. Hudson, R. Rahman, A. S. Dzurak, and A. Saraiva, Bounds to electron spin qubit variability for scalable cmos architectures, *Nat. Commun* **15**, 4299 (2024).
- [60] J. R. Petta, A. C. Johnson, J. M. Taylor, E. A. Laird, A. Yacoby, M. D. Lukin, C. M. Marcus, M. P. Hanson, and A. C. Gossard, Coherent manipulation of coupled electron spins in semiconductor quantum dots, *Science* **309**, 2180 (2005).
- [61] M. Lodari, N. W. Hendrickx, W. I. L. Lawrie, T.-K. Hsiao, L. M. K. Vandersypen, A. Sammak, M. Veldhorst, and G. Scappucci, Low percolation density and charge noise with holes in germanium, *Materials for Quantum Technology* **1**, 011002 (2021).
- [62] B. Paquelet Wuetz, D. Degli Esposti, A.-M. J. Zwerver, S. V. Amitonov, M. Botifoll, J. Arbiol, A. Sammak, L. M. K. Vandersypen, M. Russ, and G. Scappucci, Reducing charge noise in quantum dots by using thin silicon quantum wells, *Nature Communications* **14**, 1385 (2023).
- [63] S. M. Patomäki, M. F. Gonzalez-Zalba, M. A. Fogarty, Z. Cai, S. C. Benjamin, and J. J. L. Morton, Pipeline quantum processor architecture for silicon spin qubits, *npj Quantum Inf* **10**, 31 (2024).
- [64] P. Stano and D. Loss, Review of performance metrics of spin qubits in gated semiconducting nanostructures, *Nature Reviews Physics* **4**, 672 (2022).
- [65] J. Heinsoo, C. K. Andersen, A. Remm, S. Krinner, T. Walter, Y. Salathé, S. Gasparinetti, J.-C. Besse, A. Potočník, A. Wallraff, and C. Eichler, Rapid high-fidelity multiplexed readout of superconducting qubits, *Phys. Rev. Appl.* **10**, 034040 (2018).
- [66] P. Steinacker, N. D. Stuyck, W. H. Lim, T. Tanttu, M. Feng, A. Nickl, S. Serrano, M. Candido, J. D. Cifuentes, F. E. Hudson, K. W. Chan, S. Kubicek, J. Jusot, Y. Canvel, S. Beyne, Y. Shimura, R. Loo, C. Godfrin, B. Raes, S. Baudot, D. Wan, A. Laucht, C. H. Yang, A. Saraiva, C. C. Escott, K. D. Greve, and A. S. Dzurak, A 300 mm foundry silicon spin qubit unit cell exceeding 99% fidelity in all operations (2024), [arXiv:2410.15590 \[cond-mat.mes-hall\]](https://arxiv.org/abs/2410.15590).
- [67] A. J. Sigillito, M. J. Gullans, L. F. Edge, M. Borselli, and J. R. Petta, Coherent transfer of quantum information in a silicon double quantum dot using resonant swap gates, *npj Quantum Information* **2019 5:1** **5**, 1 (2019).
- [68] F.-E. von Horstig, D. J. Ibberson, G. A. Oakes, L. Cochrane, D. F. Wise, N. Stelmashenko, S. Barraud, J. A. Robinson, F. Martins, and M. F. Gonzalez-Zalba, Multimodule microwave assembly for fast readout and charge-noise characterization of silicon quantum dots, *Phys. Rev. Appl.* **21**, 044016 (2024).
- [69] I. Ahmed, J. A. Haigh, S. Schaal, S. Barraud, Y. Zhu, C. min Lee, M. Amado, J. W. A. Robinson, A. Rossi, J. J. L. Morton, and M. F. Gonzalez-Zalba, Radio-frequency capacitive gate-based sensing, *Phys. Rev. Appl.* **10**, 014018 (2018).
- [70] L. Kranz, S. K. Gorman, B. Thorgrimsson, Y. He, D. Keith, J. G. Keizer, and M. Y. Simmons, Exploiting a single-crystal environment to minimize the charge noise on qubits in silicon, *Advanced Materials* **32**, 2003361 (2020).
- [71] W. G. van der Wiel, S. D. Franceschi, J. M. Elzerman, T. Fujisawa, S. Tarucha, and L. P. Kouwenhoven, Electron transport through double quantum dots, *Rev. Mod. Phys.* **75**, 1 (2002).
- [72] R. Mizuta, R. M. Otxoa, A. C. Betz, and M. F. Gonzalez-Zalba, Quantum and tunneling capacitance in charge and spin qubits, *Phys. Rev. B* **95**, 045414 (2017).
- [73] T. Lundberg, J. Li, L. Hutin, B. Bertrand, D. J. Ibberson, C.-M. Lee, D. J. Niegemann, M. Urdampilleta, N. Stelmashenko, T. Meunier, J. W. A. Robinson, L. Ibberson, M. Vinet, Y.-M. Niquet, and M. F. Gonzalez-Zalba, Spin quintet in a silicon double quantum dot: Spin blockade and relaxation, *Phys. Rev. X* **10**, 041010 (2020).

| Reference | Platform | Resonator | τ_{int} (μs) | \mathcal{F}_r (%) | T_1 (μs) |
|----------------------------------|----------------------------|-------------|---------------------------------------|---------------------|-------------------------|
| Pakkiam <i>et al.</i> 2018 [32] | Donor in Si | Off-chip SC | 300 | 82.9 | 620 |
| West <i>et al.</i> 2019 [33] | Planar Si/SiO ₂ | SMD | 2000 | 73.3 | 4500 |
| Zheng <i>et al.</i> 2019 [34] | Si/SiGe | On-chip SC | 6 | 98.0 | 159 |
| Chittock-Wood <i>et al.</i> 2025 | Planar Si/SiO ₂ | Off-chip SC | 8 | 67.0 | 24 |

Supplementary Table I. In-situ dispersive readout performance across different silicon technology platforms. Here resonators are categorised into three-types, on- and off-chip superconducting (SC) resonators and those constructed using surface mounted (SMD) circuit components.

| Reference | Platform | $\delta\epsilon_{\text{rms}}$ (μeV) | $\Delta E_{z,\text{rms}}$ (neV) | T_2^* (μs) | T_2^{echo} (μs) | $T_{2,\text{mag}}^*$ (μs) |
|----------------------------------|-----------------------------------|--|---------------------------------|---------------------------|---------------------------------------|--|
| Jock <i>et al.</i> 2018 [26] | ²⁸ Si/SiO ₂ | 2.0 | $\leq 0.2^a$ | 1.00 | 8.4 | ≥ 20 |
| Connors <i>et al.</i> 2022 [56] | Si/SiGe | 2.7 | $\leq 1.3^b$ | 0.10 | 0.4 | ≥ 9 |
| Chittock-Wood <i>et al.</i> 2025 | Si/SiO ₂ | 5.4 | 3.4 | 0.04 | 0.4 | 3 |

Supplementary Table II. Exchange echo reports in silicon quantum devices, where a singlet-triplet qubit is configured to dephase under exchange J and is refocused via the difference in Zeeman energy between the two dots ΔE_z [47] (in a DQD). Noise parameters $\delta\epsilon_{\text{rms}}$ and $\delta\Delta E_{z,\text{rms}}$ describe rms fluctuations in detuning ϵ and ΔE_z , respectively. Note that here, the dephasing time T_2^* listed does not represent the longest T_2^* achieved in each reference, but is the reported value at the detuning ϵ_{echo} where the echo was implemented. The echo time is reported as T_2^{echo} , and this is contrasted against the magnetic limited dephasing time $T_{2,\text{mag}}^* = \lim_{\delta\epsilon_{\text{rms}} \rightarrow 0} T_2^*$, $^{a-b}$ determined by $\sqrt{2}\hbar / \lim_{\epsilon \rightarrow \infty} T_2^*$ in a Fig. 4(d) [26] and b Fig. 2(d) [56].